Convective instabilities in a laminar shock-wave/boundary-layer interaction

Niessen, Sébastien E.M.; Groot, Koen J.; Hickel, Stefan; Terrapon, Vincent E.

DOI
10.1063/5.0135590

Publication date
2023

Document Version
Final published version

Published in
Physics of Fluids

Citation (APA)
Niessen, S. E. M., Groot, K. J., Hickel, S., & Terrapon, V. E. (2023). Convective instabilities in a laminar shock-wave/boundary-layer interaction. *Physics of Fluids*, *35*(2), Article 024101. https://doi.org/10.1063/5.0135590

Important note
To cite this publication, please use the final published version (if applicable).
Please check the document version above.

Physics of Fluids

Convective instabilities in a laminar shock-wave/boundary-layer interaction

Cite as: Phys. Fluids **35**, 024101 (2023); https://doi.org/10.1063/5.0135590
Submitted: 21 November 2022 • Accepted: 11 January 2023 • Published Online: 02 February 2023

Sébastien E. M. Niessen, Koen J. Groot, Stefan Hickel, et al.

Physics of Fluids ARTICLE scitation.org/journal/phf

Convective instabilities in a laminar shock-wave/boundary-layer interaction

Cite as: Phys. Fluids **35**, 024101 (2023); doi: 10.1063/5.0135590
Submitted: 21 November 2022 · Accepted: 11 January 2023 ·
Published Online: 2 February 2023

Sébastien E. M. Niessen,[1,a] Koen J. Groot,[2,a] Stefan Hickel,[3,b] and Vincent E. Terrapon[1,a]

AFFILIATIONS

[1]Aerospace & Mechanical Engineering, University of Liège, Liège 4000, Belgium
[2]Department of Aerospace Engineering, Texas A&M University, College Station, Texas 77843, USA
[3]Faculty of Aerospace Engineering, Delft University of Technology, Delft 2629HS, The Netherlands

[a]Electronic mail: sebastien.niessen@gmail.com; koengroot90@gmail.com and vincent.terrapon@uliege.be
[b]Author to whom correspondence should be addressed: s.hickel@tudelft.nl

ABSTRACT

Linear stability analyses are performed to study the dynamics of linear convective instability mechanisms in a laminar shock-wave/boundary-layer interaction at Mach 1.7. In order to account for all two-dimensional gradients elliptically, we introduce perturbations into an initial-value problem that are found as solutions to an eigenvalue problem formulated in a moving frame of reference. We demonstrate that this methodology provides results that are independent of the numerical setup, frame speed, and type of eigensolutions used as initial conditions. The obtained time-integrated wave packets are then Fourier-transformed to recover individual-frequency amplification curves. This allows us to determine the dominant spanwise wavenumber and frequency yielding the largest amplification of perturbations in the shock-induced recirculation bubble. By decomposing the temporal wave-packet growth rate into the physical energy-production processes, we provide an in-depth characterization of the convective instability mechanisms in the shock-wave/boundary-layer interaction. For the particular case studied, the largest growth rate is achieved in the near-vicinity of the bubble apex due to the wall-normal (productive) and streamwise (destructive) Reynolds-stress energy-production terms. We also observe that the Reynolds heat-flux effects are similar but contribute to a smaller extent.

I. INTRODUCTION

Shock-wave/boundary-layer interaction (SWBLI) is a ubiquitous phenomenon in high-speed aerodynamics that significantly impacts aircraft performance by, for instance, promoting laminar–turbulent transition, causing excessive heating of aerodynamic surfaces, and creating pressure losses in engine intakes or even local fatigue of the solid structures.[1] SWBLI is present in applications ranging from the transonic to hypersonic regime, and a comprehensive understanding of its physics is required to devise effective and efficient high-speed vehicles.

The first observations of SWBLI were made on airfoils by Ferri[2] and, shortly later, thorough experimental studies have been published with normal,[3] compression-ramp,[4,5] and near-normal/oblique[6] shock waves. Since then, SWBLI has been extensively studied over numerous flow configurations; the progress accomplished over the past decades has been reviewed by, for example, Délery *et al.*,[7] Dolling,[8] Babinsky and Harvey,[9] and Gaitonde.[10] Considerable efforts have been invested to reveal the mechanisms governing the unsteadiness of the SWBLI, such as breathing of the recirculation bubble, oscillations of the shock system, or laminar–turbulent transition, but comprehensive research is still required to understand these phenomena.

The unsteadiness of the SWBLI often refers to low-frequency oscillations of the interaction region.[8] Numerous computational and numerical investigations have been conducted to determine the physical mechanisms at the origin of this unsteadiness and have led to a classification of the mechanisms into two main categories. On the one hand, Beresh *et al.*,[11] Ganapathisubramani *et al.*,[12,13] and Wu and Martín[14] suggested that the SWBLI acts as an amplifier of upstream incoming disturbances that enter the shock-induced separated boundary layer. Recent studies have also demonstrated the importance of what is referred to as an upstream-influence shock,[15–18] an oscillating shock that is located far upstream of the interaction and whose frequency content could be correlated with the unsteadiness of the shock-induced bubble. The related studies rely on the statistical correlation of the incoming perturbations and the low-frequency response

of the interaction region. However, this approach does not seem applicable for all cases as, for example, Wu and Martín[14] did not find a significant correlation in one of their configurations. On the other hand, Touber and Sandham,[19,20] Pirozzoli and Grasso,[21] Dussauge *et al.*,[22] Piponniau *et al.*,[23] Grilli *et al.*,[24] Sansica *et al.*,[25] Pasquariello *et al.*,[26] Adler and Gaitonde,[27] and Sasaki *et al.*[28] showed evidence of mechanisms that have a more intrinsic character. In fact, this second theory indicates that a feedback mechanism can cause downstream disturbances, present in the aft-shock region, to be entrained and amplified within the recirculation bubble. In turbulent SWBLI, Clemens and Narayanaswamy[29] have suggested that the two types of mechanisms are always present together, with the intrinsic one becoming more dominant as the separation region increases. In laminar/transitional SWBLI, Sansica *et al.*,[25] Dwivedi *et al.*,[30] Bonne *et al.*,[31] and Bugeat *et al.*[32] suggest that the low-frequency unsteadiness is not a self-sustained mechanism and thus needs to be forced. However, since the interaction region acts as a low-pass spatial amplification filter,[25,32] the low-frequency oscillations do not need to be forced necessarily at a low frequency. Furthermore, Sansica *et al.*[25] and Bonne *et al.*[31] argued that the low-frequency oscillations can originate from upstream traveling waves that are triggered by instability mechanisms or a laminar–turbulent transition process taking place in the downstream portion of the interaction region. Ultimately, although remarkable progress has been made during the past decade, no consensus has been reached regarding the origin of this unsteadiness. With the present paper, we address the origin of unsteady instability mechanisms that are supported by laminar SWBLI by considering an advanced linear instability approach that does not restrict the analysis to a particular instability mechanism.

Several instability mechanisms in laminar and turbulent SWBLI have been investigated in past studies. Among all of them, global mechanisms are of particular interest because they represent localized modes that are intrinsic to the interaction region. Oscillatory global modes at the origin of the low-frequency breathing and the downstream vortex shedding were found by Nichols *et al.*[33] and Pirozzoli *et al.*[34] in turbulent SWBLI. However, in laminar (shock-induced) separation bubbles, only a global *stationary* mode has been found so far,[35–37] that is responsible for a two (2D)-to-three-dimensional (3D) topological change of the separation bubble. Although Robinet[35] suggested that a three-dimensional bubble is a prerequisite for the low-frequency oscillations in laminar SWBLI, the non-oscillatory global instability mechanism cannot be held responsible for sustaining the unsteadiness. In this sense, Guiho *et al.*[38] concluded that laminar SWBLIs in a broad range of conditions are globally stable, and thus, convective instability mechanisms should be considered. Such mechanisms propagate the perturbations away from the initial location of the disturbance and have been found by Sansica *et al.*,[25] Dwivedi *et al.*,[30] Hildebrand *et al.*,[36] Guiho *et al.*,[38] Yao *et al.*,[39] Sansica *et al.*,[40] and Bugeat *et al.*[32] with different computational approaches.

Convective instabilities in laminar SWBLI were considered by Yao *et al.*[39] and Sansica *et al.*[40] through the response of the flow to external forcing with direct numerical simulations (DNS) and/or large-eddy simulations (LES). However, these methods require judicious initial conditions or forcing to perturb the (convectively unstable) flow and their relatively high computational cost restricts the study of the perturbation dynamics to a limited range of forcing configurations. This limitation is circumvented when considering linear stability methods that are less expensive and, due to their linearity, yield results that do not depend on the magnitude of the initial condition or forcing. Hence, Yao *et al.*[39] and Sansica *et al.*[25] relied on linear stability theory (LST) and parabolized stability equation (PSE) approaches to examine the growth of perturbations through convective instability mechanisms in laminar SWBLI. While the stability results are in good agreement with DNS for weak oblique shocks, these studies also highlight the limitations of LST and PSE in the case of a strong interaction. The parallel and slow-evolution assumptions, on which the LST and PSE methods, respectively, rely, do not allow accurately capturing instability information in flows with rapid streamwise variations. Furthermore, although streamwise variations are better captured by PSE, the parabolized formulation of the equations in the streamwise direction prevents capturing the upstream response to downstream forcing. Hence, to account for all effects in the plane-parallel to the streamwise direction, that is, in the plane where the separation bubble is highly two-dimensional, a formulation of the stability equations that allows a fully elliptic representation of the convective instabilities is needed.

The eigenvalue-problem formulation of the two-dimensional linear stability equations allows obtaining a fully elliptic representation of the perturbations without restricting the dynamics to a particular forcing or initial condition. When applied to streamwise developing flows, the method is referred to as the streamwise BiGlobal stability problem.[41,42] This approach is particularly suitable to identify instability mechanisms in SWBLI and yielded different outcomes in the past. On the one hand, Pirozzoli *et al.*,[34] Robinet,[35] and Nichols *et al.*[33] have highlighted the presence of the previously described *global* instability mechanisms that are localized in the shock-induced separation bubble. On the other hand, Guiho *et al.*[38] have identified *convective* instability mechanisms that can be activated by external perturbations entering the bubble before being swept away by the flow. However, when these convective instabilities are sought in a stationary frame of reference, the corresponding results suffer from a notorious numerical sensitivity,[43–45] especially with respect to the streamwise truncation boundaries, that is, domain length, boundary conditions, and streamwise discretization. Hence, having not found unstable global modes, Guiho *et al.*[38] only concluded that their laminar SWBLI is globally stable and that the stationary-frame eigensolutions corresponding to convective instabilities are tainted by the sensitivity with respect to the truncation boundaries, which introduces a bias in the characterization of the physical mechanisms.[46]

The present study aims to improve the characterization of the three-dimensional convective instability mechanisms in a two-dimensional laminar SWBLI flow. To this end, we disturb an initial-value problem with initial conditions that are solutions of the elliptic, linear stability equations formulated in a moving frame of reference. The methodology was used in the past by Mittal and Kumar,[47] Mittal *et al.*,[48] and Kumar and Mittal[49] to study convective instability mechanisms in a cylinder wake and accounts for all in-plane gradients without restricting the perturbation dynamics to a particular forcing or initial condition. Furthermore, we observe that this computational approach eliminates the sensitivity issues related to the streamwise truncation boundaries. For the present work, this method allows us to identify the frequencies and spanwise wavenumbers yielding the largest spatial amplification across the shock-induced bubble. Furthermore, by having setup-independent solutions, we can

characterize the physical mechanisms governing the convective instabilities in the laminar SWBLI flow in detail.

The paper is structured as follows. In Sec. II, the governing equations and the flow configuration are presented along with the selective frequency damping (SFD) method that is used to obtain the base flow. As part of the SFD and stability results, we demonstrate that no 2D and 3D global instability mechanisms are supported by the present flow, respectively. Hence, we focus on convective instability mechanisms. The methodology to study this type of instabilities is introduced in Sec. III. Different tools to characterize the spatiotemporal evolution of the perturbations are also presented in this section. Finally, the results of the stability analyses are discussed in Sec. IV. In particular, the mechanisms yielding the largest amplification of perturbations in the present SWBLI are identified and then characterized by decomposing the material derivative of the perturbation energy into the individual physical mechanisms.

II. BASE-FLOW CONFIGURATION AND GOVERNING EQUATIONS

A. Compressible Navier–Stokes equations

The physical problem is governed by the three-dimensional compressible Navier–Stokes equations

$$\frac{\partial \rho}{\partial t_\mathrm{f}} + \frac{\partial \rho u_j}{\partial x_{\mathrm{f},j}} = 0, \tag{1a}$$

$$\frac{\partial \rho u_i}{\partial t_\mathrm{f}} + \frac{\partial \rho u_j u_i}{\partial x_{\mathrm{f},j}} = -\frac{\partial p}{\partial x_{\mathrm{f},i}} + \frac{1}{\mathrm{Re}}\frac{\partial \tau_{ij}}{\partial x_{\mathrm{f},j}}, \tag{1b}$$

$$\frac{\partial E}{\partial t_\mathrm{f}} + \frac{\partial}{\partial x_{\mathrm{f},j}}\left[(E+p)u_j\right] = \frac{1}{\mathrm{Re}}\frac{\partial}{\partial x_{\mathrm{f},j}}\left[\tau_{ij}u_i - \frac{\kappa}{\mathrm{Pr}\,\mathrm{Ec}}\frac{\partial T}{\partial x_{\mathrm{f},j}}\right], \tag{1c}$$

with ρ the density, p the pressure, u_i the three velocity components, and E the total energy. The subscript "f" refers to a stationary frame of reference. Equation (1) is written in a non-dimensional form. The Mach (M), Reynolds (Re), Prandtl (Pr), and Eckert (Ec) numbers are defined as

$$\mathrm{M} \overset{(a)}{=} \frac{u_e}{\sqrt{\gamma R T_{e,\mathrm{static}}}}, \quad \mathrm{Re}_\mathfrak{L} \overset{(b)}{=} \frac{\rho_e u_e \mathfrak{L}}{\mu_e}, \quad \mathrm{Pr} \overset{(c)}{=} \frac{c_p \mu_e}{\kappa_e}, \quad \mathrm{Ec} \overset{(d)}{=} \frac{u_e^2}{c_p T_{e,\mathrm{static}}}, \tag{2}$$

based on freestream quantities (indicated by subscript e). The length $\mathfrak{L}$, which is specified as a subscript of Re, denotes a generic characteristic length scale. We introduce $\ell = \mu_e/\rho_e u_e$ as our global length scale, so that $\mathrm{Re} = \mathrm{Re}_\ell = \rho_e u_e \ell/\mu_e = 1$ in Eqs. (1b) and (1c). We consider a perfect gas with the specific gas constant of air $R = 287\,[\mathrm{J/(kg\,K)}]$ and $\gamma = c_p/c_v = 1.4$, where c_p and $c_v = c_p - R$ are the isobaric and isochoric heat capacities. The heat transfer in the energy Eq. (1c) is modeled with Fourier's law and, thus, relies only on thermal conductivity κ and temperature T. Furthermore, we assume that the fluid is Newtonian (with Stokes' hypothesis). This allows writing the shear-stress tensor τ_{ij}, the total energy E, and the ideal-gas equation as

$$\tau_{ij} = \mu\left(\frac{\partial u_i}{\partial x_{\mathrm{f},j}} + \frac{\partial u_j}{\partial x_{\mathrm{f},i}}\right) - \frac{2}{3}\mu\frac{\partial u_k}{\partial x_k}\delta_{ij}, \tag{3a}$$

$$E = \rho\left(\frac{T}{\gamma(\gamma-1)\mathrm{M}^2} + \frac{1}{2}u_i u_i\right), \tag{3b}$$

$$p = \rho R T. \tag{3c}$$

The dynamic viscosity μ and the thermal conductivity κ are assumed to depend exclusively on the temperature and are modeled by Sutherland's law

$$\mu = \mu(T) = \mu_\mathrm{ref}\left(\frac{T}{T_\mathrm{ref}}\right)^{\frac{3}{2}}\frac{T_\mathrm{ref}+S}{T+S}, \tag{4a}$$

$$\kappa = \frac{c_p}{\mathrm{Pr}}\mu, \tag{4b}$$

with constant parameters $\mu_\mathrm{ref} = 1.716\times10^{-5}\,[\mathrm{kg/(m\,s)}]$, $S = 110.4\,\mathrm{K}$, $T_\mathrm{ref} = 273.15\,\mathrm{K}$, and $\mathrm{Pr} = 0.72$.

B. Flow configuration

The flow considered in the present study consists of an incident shock that impinges on a laminar flat-plate boundary layer (Fig. 1). Experimental measurements of a similar flow (differences will be detailed shortly) have been conducted by Giepman[50] for various shock-wave angles, impinging locations and regimes of the incoming boundary layers. For the present numerical analyses, we selected one flow configuration for which the laminar–turbulent transition occurs downstream of the incident shock. The main setup parameters are summarized in Table I. The incoming laminar boundary layer enters the numerical domain at $x_{\mathrm{f},0}/\ell = \mathrm{Re}_{x_{\mathrm{f},0}} = 7\times10^5$ with displacement thickness $\delta_0/\ell = \mathrm{Re}_{\delta_0} = 5073$. The freestream Mach and unit Reynolds numbers are $\mathrm{M} = 1.7$ and $\mathrm{Re}_e = 1/\ell = 3.5\times10^7\,\mathrm{m}^{-1}$, respectively. The incident shock is generated in the freestream with a 2° wedge, has an angle $\theta_\mathrm{incident} = 37.93°$, and impinges on the laminar boundary layer at $x_\mathrm{imping.}/\ell = \mathrm{Re}_{x_\mathrm{imping.}} = 1.785\times10^6$. The measurements by Giepman[50] indicate that the laminar–turbulent transition takes place as a consequence of the perturbation development in the SWBLI. When using a computational approach to simulate the flow field without an artificial/numerical stabilization technique, this particular unsteadiness prevents the simulation from reaching a laminar steady state. The specific experimental conditions feature a wall-temperature distribution that varies in time. To avoid complications introduced by such a boundary condition, and because no further information about perturbations is provided by the experiment anyway, a close but more canonical case is considered here, in which the wall is assumed to be adiabatic.

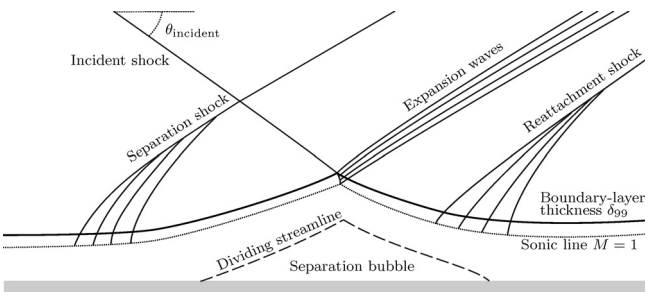

FIG. 1. Schematic of shock-wave/boundary-layer interaction with laminar separation bubble.

TABLE I. Flow parameters of laminar shock-wave/boundary-layer interaction.

M	u_e [m/s]	Ec	$T_{e,\text{total}}$ [K]	$p_{e,\text{static}}$ [Pa]	Re_e [1/m]	Re_{x_0}	Re_{δ_0}	$\text{Re}_{x_{\text{imping.}}}$	θ_{incident}
1.7	452.12	1.156	277.73	2.3×10^5	3.5×10^7	7×10^5	5073	1.785×10^6	37.93°

C. Numerical setup

The flow is obtained by solving the compressible Navier–Stokes equations via finite-volume direct numerical simulations.[51] The time-integration is achieved with an explicit fourth-order Runge–Kutta scheme and the temporal resolution is fixed by a global time step such that the Courant–Friedrichs–Lewy condition CFL < 1 is satisfied for each grid point in the domain. We use a Cartesian structured grid that is uniform in the streamwise direction x with N_x points and the domain length for the base flow is $L/\ell = 2.5365 \times 10^6$. In the wall-normal direction y, the grid is stretched with a hyperbolic function in order to cluster grid points near the wall in the shear-layer region ($\Delta y^+ < 1$) and around the shock-impingement location. The domain height is $H/\ell = 0.760\,95 \times 10^6$, that is, 150 times the boundary-layer height at the inlet. The convective fluxes are evaluated with a third-order weighted essentially non-oscillatory (WENO) scheme coupled with the Harten–Lax–van Leer contact (HLLC) Riemann solver. The viscous fluxes are computed with a second-order central difference scheme. The effectiveness of the present flux-reconstruction method in obtaining non-oscillatory SWBLI flows has been assessed by Niessen.[52]

The boundary conditions are imposed as follows. A compressible flat-plate boundary-layer profile is prescribed at the inlet and the incident oblique shock, emanating from the upper boundary, is imposed by a Rankine–Hugoniot condition. The solid wall ($y = 0$) is an adiabatic surface on which the no-slip condition for the velocities is enforced (i.e., $u_i = 0$). At the outflow, a homogeneous Neumann condition in the streamwise direction governs all variables. To avoid reflections on the domain borders, we use Riemann-invariant-based non-reflective conditions at all truncation boundaries.

D. Steady-state solution: Selective frequency damping method

Stability analysis relies on the evolution of perturbations around a laminar equilibrium solution of the governing equations that needs to be determined beforehand. This so-called base-flow solution, given by the flow variable $\bar{\boldsymbol{Q}}$, satisfies the steady Navier–Stokes equations, that is,

$$\frac{\partial \bar{\boldsymbol{Q}}}{\partial t_\text{f}} = \mathcal{N}(\bar{\boldsymbol{Q}}) = 0, \tag{5}$$

with $\mathcal{N}$ the nonlinear, steady Navier–Stokes operator. In order to drive the unsteady flow field $\boldsymbol{q}$ toward $\bar{\boldsymbol{Q}}$, we presently rely on the selective frequency damping (SFD) method.[53–55] The SFD approach contrasts with past stability analyses carried out on laminar SWBLI,[25,35,36,38–40,56] which used long-time nonlinear saturation of two-dimensional DNS to obtain stable steady-state base-flow solutions. This latter approach to obtain the laminar base flow is effective solely when the considered laminar flow is stable to all two-dimensional perturbations. For the present case, the flow configuration contains a strong shock-induced separation region with laminar–turbulent transition downstream of the separation-bubble apex, which thus prevents reaching a steady-state naturally. By considering the SFD approach, the instability mechanisms triggering the transition can be damped out, and thus, upon achieving a negligible residual, we obtain an accurate steady-state base-flow solution that is inherently unstable.

In the SFD approach, a source term is introduced into the Navier–Stokes equations (1) that is proportional to the high-frequency content $(\boldsymbol{q} - \boldsymbol{q}_\text{lf})$ of the flow. The field $\boldsymbol{q}_\text{lf}$ represents a low-pass filtered version of the flow field $\boldsymbol{q}$ and serves as an approximation of the unknown base-flow solution $\bar{\boldsymbol{Q}}$. Following Åkervik *et al.*,[53] an exponential filter is chosen to calculate $\boldsymbol{q}_\text{lf}$ and the modified Navier–Stokes equations are therefore given by

$$\frac{\partial \boldsymbol{q}}{\partial t_\text{f}} = \mathcal{N}(\boldsymbol{q}) - \chi_s(\boldsymbol{q} - \boldsymbol{q}_\text{lf}), \tag{6a}$$

$$\frac{\partial \boldsymbol{q}_\text{lf}}{\partial t_\text{f}} = \frac{\boldsymbol{q} - \boldsymbol{q}_\text{lf}}{\Delta_s} \tag{6b}$$

with the positive real-valued parameters Δ_s and χ_s representing the bandwidth of the filter and the feedback control parameter, respectively. In the present case, $\chi_s \delta_0/u_e = 0.65$ and $\Delta_s u_e/\delta_0 = 1.64$ are used. The effectiveness of the SFD in driving $\boldsymbol{q}$ toward $\boldsymbol{q}_\text{lf}$ is assessed by monitoring the L_2-norm of the unsteady residual $\epsilon_s = ||\boldsymbol{q} - \boldsymbol{q}_\text{lf}||_{L_2}$. Upon driving the residual to zero, the low-pass filtered variable $\boldsymbol{q}_\text{lf}$ satisfies the steady Navier–Stokes equations and the steady-state base-flow $\bar{\boldsymbol{Q}}$ is thus given by $\boldsymbol{q}_\text{lf}$. For the present case, the residual saturates at $\mathcal{O}(10^{-9})$ as depicted in Fig. 2(a).

As thoroughly demonstrated by Casacuberta *et al.*,[55] the SFD method relies on a strategical choice of the two parameters Δ_s and χ_s to effectively and efficiently converge to low residual levels. In particular, in the presence of an unsteady, two-dimensional global mode, Casacuberta *et al.*[55] proposed the unleash technique to determine optimal coefficients that maximize the convergence rate. First, in applying this technique, we evaluate the least stable steady mode that rules the convergence rate when controlling the time-integration with the SFD forcing term ($\chi_s \neq 0$). In the present case, this steady mode corresponds to an expansion of the separation bubble [Figs. 2(b)–2(e)] with a growth rate $\omega_i \ell/u_e = -2.434 \times 10^{-8}$. Since the growth rate is negative, the flow is effectively driven toward a steady-state solution for which the bubble expansion becomes less and less dominant. Second, a white-noise perturbation of magnitude ϵ_s is superimposed to the base flow $\bar{\boldsymbol{Q}} = \boldsymbol{q}_\text{lf}$ that has been obtained at a certain low residual ϵ_s. The time-integration is then pursued with $\chi_s = 0$, that is, without the SFD forcing term. In this uncontrolled time-integration (with $\chi_s = 0$), the most unstable, two-dimensional global mode must establish with an exponential growth rate that corresponds to the slope of the temporal evolution of $||\boldsymbol{q} - \bar{\boldsymbol{Q}}||_{L_2}$. In using this technique, Casacuberta *et al.*[55] indicated that the exponential growth could be preceded by an algebraic growth that rapidly becomes overwhelmed by the

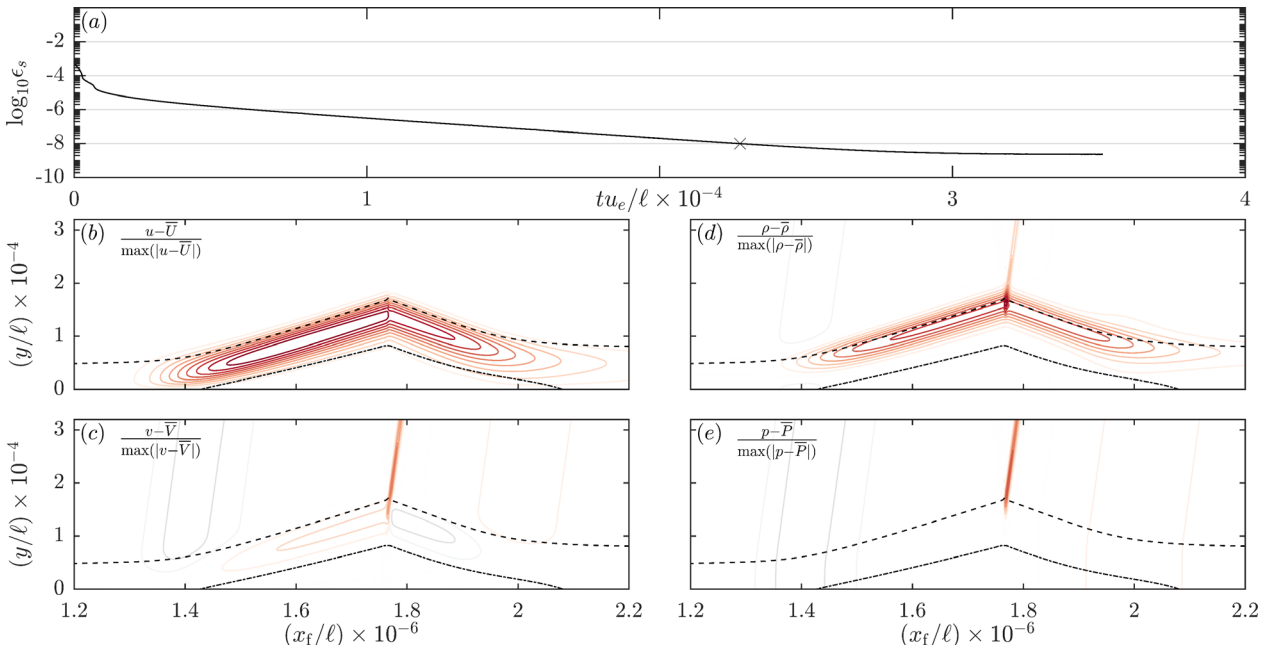

FIG. 2. (a) SFD residual $\epsilon_s = ||\mathbf{q} - \mathbf{q}_{lf}||_{L_2}/\sqrt{\mathcal{S}}$ as a function of the physical time. Perturbation shape in space when $\epsilon_s = 10^{-8}$ [indicated by $\times$ in (a)]: (b) $(u - \bar{U})/\max(|u - \bar{U}|)$; (c) $(v - \bar{V})/\max(|v - \bar{V}|)$; (d) $(\rho - \bar{\rho})/\max(|\rho - \bar{\rho}|)$; and (e) $(p - \bar{P})/\max(|p - \bar{P}|)$ [colored lines, 20 contours from minimum (−1, gray) to maximum (1, red)]. (b)–(e) Boundary-layer edge (δ_{90}, dashed); $\bar{U} = 0$ (dash-dotted).

exponential growth of the most unstable global mode, if it exists. In the present case, the unleash technique, however, reveals only an algebraic growth that is not followed by any exponential growth. This thus indicates that the present SWBLI does not support any unstable, two-dimensional global mode. Accordingly, we could not optimize the SFD coefficients with the unleash technique. Even if the parameters could not be optimized, however, the aforementioned parameters did prove to be effective.

E. Base-flow results

The density field $\bar{\rho}$ of the base flow is presented in Fig. 3(a) in which the dashed black and dash-dotted white lines indicate the boundary-layer thickness [$\delta_{90} = \delta(\bar{U} = 0.9u_e)$] and the zero-velocity ($\bar{U} = 0$) isoline, respectively. A zoom-in representation of the separation bubble is shown in Fig. 3(b) along with the velocity profiles at several streamwise locations. The dividing streamline (dotted red line) and the zero-velocity isocontour (dash-dotted black line) show that the separation region is relatively long ($L_{sep}/\ell \approx 6.50 \times 10^5$) compared to the boundary-layer thickness. The separation bubble has the typical triangular shape of laminar SWBLI, and no secondary recirculation was found for the present case. Finally, for the same flow configuration, Niessen[52] showed very good agreement with free-interaction theory.[57]

We verified that the inflow and outflow boundaries do not interact with the long separation bubble and thus do not influence the results. The Riemann boundary conditions effectively avoid reflections that would impact the interior of the domain. Finally, grid convergence of the results is demonstrated in Fig. 3(c) by means of $\partial\bar{U}/\partial y$ evaluated at the wall for three different mesh sizes. The coarsest grid consists of $N_x \times N_y = 500 \times 250$ points, with N_x and N_y the number of points in the streamwise and wall-normal directions, respectively. The intermediate grid is two times denser, and the finest grid is four times denser than the coarsest grid in both directions. The length of the separation bubble, that is, the distance between the two x-locations where $\partial\bar{U}/\partial y|_{y=0} = 0$, is $L_{sep}/\ell \times 10^{-5} = 6.36$, 6.48, and 6.50 from the least dense to the densest grid. This shows that the solution converges and that, with a further resolution increase, the difference in the separation length would be negligible. For the stability analyses, the base-flow solution on the densest grid will be used.

In the stability approach proposed in Sec. III, we will focus our attention on convective instabilities, because global instabilities are not supported by the present base flow, see Sec. II D. Two-dimensional, unsteady global modes are found not to exist by using the unleash technique of the SFD method. Three-dimensional, global modes, steady or unsteady, are neither expected nor recovered in the present computational effort; the latter will be commented on in Sec. IV A. By investigating specific characteristics of the base flow, we can synthesize expectations about three-dimensional, steady global modes based on the existing literature. According to Robinet,[35] the three-dimensional, steady global mode, associated with the spanwise modulation of the bubble, is unstable only if a secondary recirculation exists within the two-dimensional separation bubble. Since there is no secondary recirculation for the present configuration, we anticipate that the flow is globally stable. Furthermore, Avanci *et al.*[58] proposed a geometrical criterion to determine whether the separation bubble is convectively or absolutely unstable. This criterion is based on the relative position between the dividing streamline (i.e., zero-mass flux isoline) and the locus of inflection points of the streamwise velocity profile in the wall-

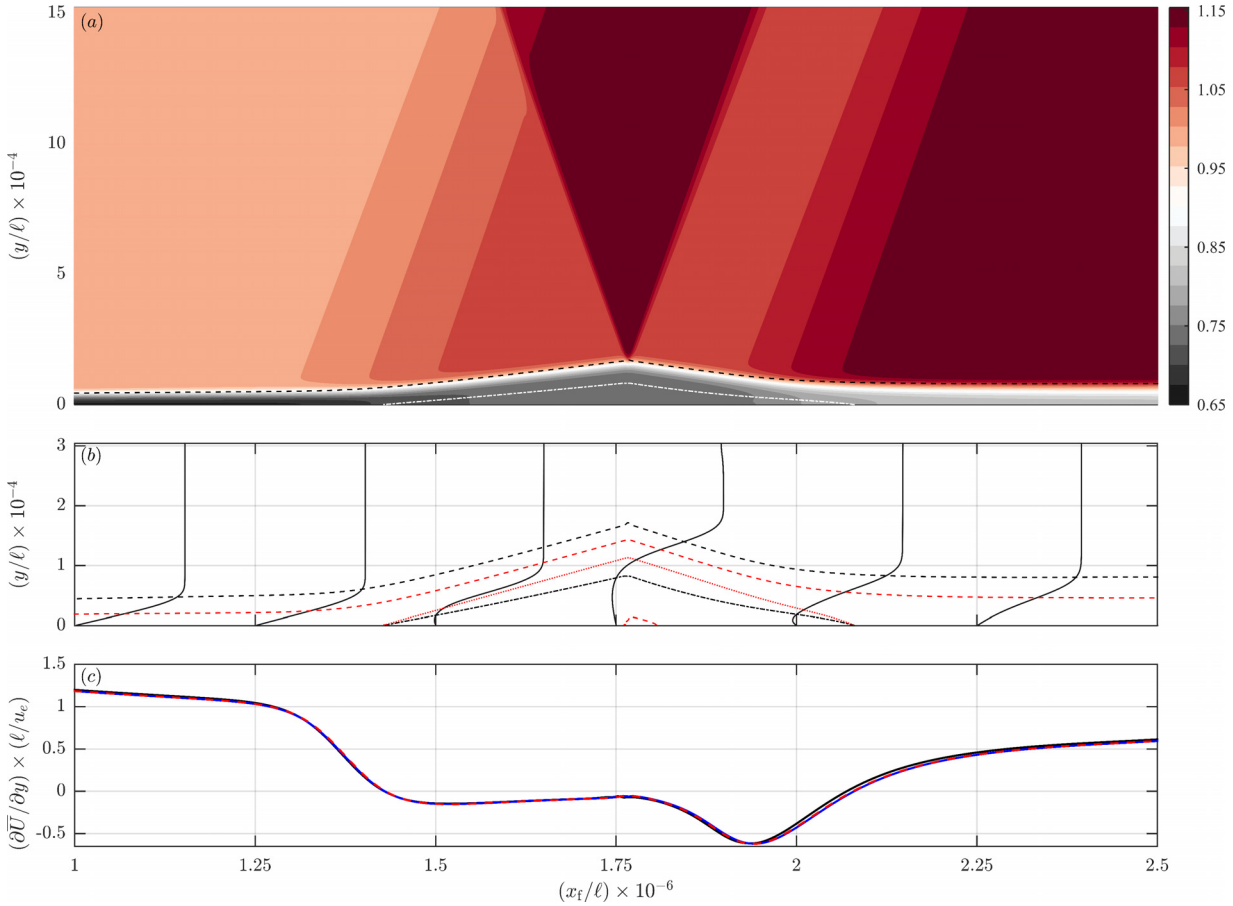

FIG. 3. (a) Isocontours of $\bar{\rho}/\rho_e$. (b) $\bar{U}/u_e$-velocity profiles, magnified by a factor 30 Re_{δ_0}, at streamwise locations $x/\ell \times 10^{-6} = 1, 1.25, 1.5, 1.75, 2, 2.25$. Locus of generalized inflection points (dashed red line) and dividing streamline (dotted red line). (a) and (b) $\delta_{90} = \delta(\bar{U} = 0.90u_e)$ in dashed black line and $\bar{U} = 0$ in dash-dotted line. (c) $\partial\bar{U}/\partial y$ evaluated at the wall for grids $N_x \times N_y = 500 \times 250$ (solid black), 1000×500 (dashed red), and 2000×1000 (solid blue).

normal direction. In particular, they showed that, for incompressible flows, upstream propagation of disturbances is expected if the inflection points $y_{\mathcal{I}}$ lie below the zero-mass-flux isoline $y_{\mathcal{D}}$ (i.e., in the region where the streamwise mass flux is negative). If this is the case, an absolute instability mechanism is expected in the separation region. For compressible flows, these locations can be defined as

$$\frac{\partial}{\partial y}\left(\bar{\rho}\frac{\partial \bar{U}}{\partial y}\right)\bigg|_{y_{\mathcal{I}}} \overset{(a)}{=} 0\,, \qquad \int_0^{y_{\mathcal{D}}} \bar{\rho}\,\bar{U}\,\mathrm{d}y \overset{(b)}{=} 0, \tag{7}$$

and are shown in Fig. 3(b). We observe that the wall-normal coordinate of the dividing streamline $y_{\mathcal{D}}$ (dotted red line) is located below the generalized inflection point $y_{\mathcal{I}}$ (dashed red line) for the present case. Hence, upon extrapolating the criterion to the compressible regime, we expect that the flow is not absolutely unstable but rather solely exhibits convective instability mechanisms.

III. METHODOLOGY FOR INSTABILITY ANALYSIS

In order to accurately describe the convective instability mechanisms supported by the present steady-state base flow, we will analyze the spatiotemporal evolution of perturbations across the shock-induced bubble. To this end, we use the linear perturbation equations formulated in the stationary frame of reference.

A. Linear perturbation equations

Stability analysis relies on examining the evolution of disturbances that are superimposed on the laminar base-flow field. The instantaneous field $\boldsymbol{q}$ is defined as the sum of the base flow $\bar{\boldsymbol{Q}}$, satisfying the steady Navier–Stokes equations $\mathcal{N}(\bar{\boldsymbol{Q}}) = 0$, and an infinitesimally small disturbance $\boldsymbol{q}'_{\mathrm{f}}$,

$$\boldsymbol{q}_{\mathrm{f}}(x_{\mathrm{f}}, y, z, t_{\mathrm{f}}) = \bar{\boldsymbol{Q}}(x_{\mathrm{f}}, y) + \boldsymbol{q}'_{\mathrm{f},r}(x_{\mathrm{f}}, y, z, t_{\mathrm{f}}), \tag{8}$$

where the subscript r indicates taking the real part of a complex-valued variable. The need for a disturbance $\boldsymbol{q}'_{\mathrm{f}}$ that is a complex-valued variable is inherited from the initial conditions that we establish in Sec. III B. The subscript f is not used for y and z, because the frame will only be moved in the streamwise direction. Note that the base flow presently considered is two-dimensional and has thus no dependency on the z direction. The perturbations are, however, allowed to

depend on z. The vector $\boldsymbol{q}'_{\mathrm{f}}$ contains the perturbation variables corresponding to each individual component of the base flow, that is, $\boldsymbol{q}'_{\mathrm{f}} = [u', v', w', T', \rho']^{\mathrm{T}}$. Introducing the decomposition (8) into the Navier–Stokes equations (1) and retaining only the first-order terms in $\boldsymbol{q}'_{\mathrm{f}}$ yields the governing equations of the linear perturbations

$$\mathcal{B}(\bar{\boldsymbol{Q}})\frac{\partial \boldsymbol{q}'_{\mathrm{f}}}{\partial t_{\mathrm{f}}} = \mathcal{A}_z(\bar{\boldsymbol{Q}})\boldsymbol{q}'_{\mathrm{f}}. \tag{9}$$

The operators $\mathcal{A}_z$ and $\mathcal{B}$ are obtained from the linearized version of the Navier–Stokes operator $\mathcal{N}$ and, in their discrete form, are matrices with coefficients containing base-flow variables $\bar{\boldsymbol{Q}}$ and discretized spatial derivative operators. The perturbation equations (9) form an initial-value problem that can be integrated in time for any initial condition. In order to resolve the perturbation evolution accurately in time, a four-step Runge–Kutta scheme is considered in this work.

The challenging aspect of solving the initial-value problem lies in the appropriate choice of initial conditions/forcing that will activate the most critical instability mechanisms. In this regard, different approaches can be found in the literature. Using singular value decomposition (SVD) would allow us to seek the continuous/initial forcing that maximizes the perturbation growth, at the cost of revealing only specific optimal instability mechanisms. Accordingly, the related optimal growth scenarios are particular and not likely to be reproducible in an experimental context. This aspect led White[59] to highlight the importance of considering non-optimal perturbation growth and, for this reason, we avoid SVD methods in this work. Alternatively, the flow could be forced at the inlet by following the recently devised harmonic linearized Navier–Stokes (HLNS) approach.[60–64] This method accounts for all elliptic effects in the description of convective instabilities without restricting the perturbation growth to the optimal-growth scenario. However, there is no guarantee that the response is not conditioned by the forcing itself and aspects of the inherent dynamics may be occulted by the particular choice of forcing. This choice could prevent the manifestation of the inherent perturbation dynamics of the flow that is specifically targeted by the present work. Alternatively, relying on an arbitrary choice of initial conditions is practically intractable due to the infinite choice of parameters and does not ensure that the (relevant) instability mechanisms are ultimately activated. For these reasons, we prefer to initialize the linear perturbation equations with initial conditions that satisfy the linear perturbation equations in a moving frame of reference, as cast in an eigenvalue problem. The resulting eigensolutions represent the relevant, inherent dynamics of the laminar flow and, as shown later, are ideal candidates for the initial conditions.

B. Initial conditions

We initialize equations (9) with initial conditions of the form:

$$\boldsymbol{q}'_{\mathrm{f}}(x_{\mathrm{f}}, y, z, t_{\mathrm{f}}) = \tilde{\boldsymbol{q}}(x_{\mathrm{f}} - c_{\mathrm{f}} t_{\mathrm{f}}, y)\mathrm{e}^{\mathrm{i}(\beta z - \omega t_{\mathrm{f}})} \quad \text{as } t_{\mathrm{f}} \to 0. \tag{10}$$

That is, a function:

1. whose shape $\tilde{\boldsymbol{q}}$ is invariant in a plane that is spanned by the streamwise and wall-normal coordinates and that *moves* in the streamwise direction with a constant frame speed c_{f};
2. that is otherwise a complex exponential in time t_{f} and the homogeneous spatial direction, that is, the spanwise z direction in this paper.

In other words, the initial condition naturally resides in a moving frame with coordinates:

$$x = x_{\mathrm{f}} - c_{\mathrm{f}} t_{\mathrm{f}}, \quad t = t_{\mathrm{f}}. \tag{11}$$

In this moving frame, the real part of ω, ω_r, represents the frequency of oscillations, while its imaginary part, ω_i, is the temporal growth rate ($\omega_i > 0$ for growth). The real-valued β represents the wavenumber in the spanwise z direction; $\lambda_z = 2\pi/\beta$ is the related wavelength.

Substituting Eqs. (10) and (11) into (9) yields

$$\left(\mathcal{A}_\beta\big(\bar{\boldsymbol{Q}}(x + c_{\mathrm{f}} t, y)\big) + c_{\mathrm{f}}\mathcal{B}\frac{\partial}{\partial x}\right)\tilde{\boldsymbol{q}}(x, y) = -\mathrm{i}\omega\mathcal{B}\tilde{\boldsymbol{q}}(x, y), \tag{12}$$

where $\mathcal{A}_\beta$ is the Fourier transform of $\mathcal{A}_z$ in z. For the present approach, the time t is treated as a *fixed* parameter to find the initial condition. Upon setting $t = 0$ in Eq. (12) and specifying c_{f}, β, and appropriate boundary conditions, it forms a (direct) eigenvalue problem for ω and $\tilde{\boldsymbol{q}}$. The component-wise form of Eq. (12) is converted from the stationary-frame equations[65] to the moving frame by replacing $\omega_{\mathrm{f}}\tilde{q}$ by $\omega\tilde{q} + \mathrm{i}c_{\mathrm{f}}\partial\tilde{q}/\partial x$ and $\partial\tilde{q}/\partial x_{\mathrm{f}}$ by $\partial\tilde{q}/\partial x$, where ω_{f} represents the angular frequency in the stationary frame of reference and $\tilde{q}$ is any component of $\tilde{\boldsymbol{q}}$.

Now consider $\boldsymbol{q}'_{\mathrm{f}}(x_{\mathrm{f}}, y, z, t_{\mathrm{f}})$, as obtained by integrating Eq. (9) while providing an initial condition satisfying Eq. (12) with $t = 0$. It immediately follows from Eq. (12) that the time-integrated $\boldsymbol{q}'_{\mathrm{f}}$ will *start to* deviate from the function on the right-hand side of Eq. (10) for non-zero $t_{(\mathrm{f})}$, because, although $\bar{\boldsymbol{Q}}$ is independent of t_{f} in the fixed frame, it does depend on t in the moving frame. Taylor-expanding the base-flow quantities in t with respect to $t = 0$,

$$\bar{\boldsymbol{Q}}(x + c_{\mathrm{f}} t, y) = \bar{\boldsymbol{Q}}(x, y) + c_{\mathrm{f}} t\frac{\partial \bar{\boldsymbol{Q}}}{\partial x_{\mathrm{f}}}(x, y) + \mathcal{O}\left(\frac{(c_{\mathrm{f}} t)^2}{2!}\frac{\partial^2 \bar{\boldsymbol{Q}}}{\partial x_{\mathrm{f}}^2}(x, y)\right), \tag{13}$$

where t is to be interpreted as an elapsed time. This indicates that the base flow can be assumed to be constant in t when permitting an error of $\mathcal{O}(c_{\mathrm{f}} t\,\partial\bar{\boldsymbol{Q}}/\partial x_{\mathrm{f}})$, which can be made negligibly small when considering small enough t. Similarly, for a small enough t, $\mathcal{A}_\beta(\bar{\boldsymbol{Q}}(x + c_{\mathrm{f}} t, y)) = \mathcal{A}_\beta(\bar{\boldsymbol{Q}}(x, y)) + \mathcal{O}(t)$, even if $\mathcal{A}_\beta = \mathcal{A}_\beta(\bar{\boldsymbol{Q}})$ is nonlinear. For this reason, the initial conditions, satisfying Eq. (12) with $t = 0$, are exact solutions of the linearized Navier–Stokes equations for the single time instant $t = 0$.

The fact that the solutions are exact at $t = 0$ contrasts with LST and PSE for which the model error exists for all times (and streamwise locations). Although the model error for the present method also relates to the streamwise derivative of the base flow, it is important to note that the model error for the present method in no way corresponds to a Wentzel–Kramers–Brillouin (WKB) approximation that underlies the LST and PSE approaches.[66–69] The present approach is fully elliptic in space, while making use of the inherent parabolic nature of the general, linearized Navier–Stokes equations *in time*.

The main motivation for such specific initial conditions is to simulate wave packets that do not depend on our truncation boundaries; these boundaries could otherwise artificially force the solution. This implies that our initial conditions should not be dominant at any of these boundaries. In other words, the eigensolutions to Eq. (12) should have eigenfunctions that are localized in the domain. More precisely,

we are looking for eigenfunctions, $\tilde{\boldsymbol{q}}$, with a negligibly small amplitude at the truncation boundaries compared to their maximum amplitude in space. In our experience,[46] eigenfunctions of eigensolutions that are representative of convective instabilities can be localized only when considering a moving frame of reference, that is, using non-zero c_f. Essentially, we argue that convective instability mechanisms are better represented as localized wave packets with a shape-invariant function that moves downstream (and grows in time) rather than as a shape-invariant function that is stationary in the streamwise direction (and grows in time). By setting $c_\mathrm{f} = 0$, one reverts Eq. (10) to the regular ansatz underlying global-mode instability analysis. If no unstable and localized global mode is found, which is determined to be the case for the presently considered base-flow configuration by a computational exploration, the classical ansatz does neither provide direct insight nor suitable, setup-independent initial conditions relevant for studying convectively unstable mechanisms.

In order to assess the sensitivity of the initial conditions with respect to the numerical setup, we also consider the adjoint eigensolutions $q^\dagger$, which solve

$$\mathcal{A}_\beta^\mathrm{H}\big(\bar{\boldsymbol{Q}}(x + c_\mathrm{f}t\,,\,y)\big)\tilde{\boldsymbol{q}}^\dagger(x,y) - c_\mathrm{f}\frac{\partial}{\partial x}\left(\mathcal{B}^\mathrm{T}\tilde{\boldsymbol{q}}^\dagger(x,y)\right) = \mathrm{i}\omega^*\mathcal{B}^\mathrm{T}\tilde{\boldsymbol{q}}^\dagger(x,y) \tag{14}$$

upon setting $t = 0$. This is referred to as the adjoint eigenvalue problem and is also formulated in the moving frame of reference. The superscripts "$*$" and "H" stand for the complex conjugate and Hermitian transpose operators, respectively. The adjoint problem (14) is based on the definition of the inner product $\langle \boldsymbol{q}_1, \boldsymbol{q}_2\rangle = \int\int \boldsymbol{q}_1^\mathrm{H}\boldsymbol{q}_2\,\mathrm{d}x\,\mathrm{d}y$.

The computational domain for stability analysis is truncated in the up- and downstream directions, at $x = x_\mathrm{in}$ and $x = x_\mathrm{out}$, and far from the flat plate at $y = y_\mathrm{max}$ ($x = 0$ corresponds to the leading edge and $y = 0$ to the wall). The truncation boundaries at $x = x_\mathrm{in}$ and $x = x_\mathrm{out}$ are, respectively, referred to as the in- and outflow boundaries. The streamwise domain length is denoted by $L = x_\mathrm{out} - x_\mathrm{in}$. We use homogeneous Neumann conditions at the in- and outflow boundaries for all perturbation variables in order to allow perturbations to be large at the boundaries if the dynamics in the interior of the domain demand it. At $y = y_\mathrm{max}$, velocity and temperature perturbations are required to vanish and the y-momentum equation is used to close the problem. The direct and adjoint eigenvalue problems are discretized with a fourth-order central finite-difference scheme in x and Chebyshev collocation[70] in y. The grid incorporates N_x and N_y discrete points in the streamwise and wall-normal directions, respectively. In the wall-normal direction y, the mapping proposed by Malik[71] is used in order to place one-half of the collocation points in $[0, y_{i,1}]$ and the other in $[y_{i,1}, y_\mathrm{max}]$ for two-dimensional perturbation solutions ($\beta = 0$). Since eigenfunctions have a slower decay and a smaller wavenumber in the wall-normal direction for two-dimensional than for three-dimensional perturbations, the Malik mapping is not suitable for solutions corresponding to non-zero β. Hence, for the three-dimensional ($\beta \neq 0$) perturbations, the collocation points in the y direction are instead mapped with the biquadratic mapping of Groot *et al.*[72] into three distinct regions $[0, y_{i,1}]$, $[y_{i,1}, y_{i,2}]$, and $[y_{i,2}, y_\mathrm{max}]$, each having one-third of the collocation points. Furthermore, the domain height for non-zero β can also be reduced because of a much faster decay of the solutions of interest in the freestream compared to the two-dimensional case. Table II summarizes the parameters used for the selected reference cases. The specific values for c_f and β presented in Table II follow from a careful exploration of the parameter space, which is discussed in Sec. IV A. Since the base-flow and stability grids are different, the base-flow solution is spline interpolated onto the grids specifically designed for the stability analysis. We verified that the solutions of the eigenvalue problem do not depend on the base-flow resolution; refining the grid by a factor two in each direction yields a relative change of order $\mathcal{O}(10^{-3})$ in the growth rate of the solutions of interest.

The solutions to eigenvalue problems (12) and (14) are obtained numerically with the Arnoldi algorithm that finds the eigensolutions of the discretized problem around a prescribed guess. The specific choice of this guess followed a thorough analysis of the spectrum to ensure that we capture the eigensolutions with the largest growth rate; that is, solutions representing the largest instantaneous growth rate supported in the considered region of the flow.

C. Global measure of time-evolving wave packets

When solving the initial-value problem (9) for time-evolving wave-packet solutions, a norm is needed to quantify the magnitude of the complex-valued disturbance as a function of time. The global measure that we will use for the general, time-dependent wave packets is the total perturbation energy

$$E(t_\mathrm{f}) = \frac{1}{2}\int\int \boldsymbol{q}_\mathrm{f}'^\mathrm{H}\mathcal{M}\boldsymbol{q}_\mathrm{f}'\,\mathrm{d}x_\mathrm{f}\,\mathrm{d}y, \tag{15}$$

where we evaluate $\boldsymbol{q}_\mathrm{f}' = [u', v', w', T', \rho']^\mathrm{T}$ at $z = 0$ and $\mathcal{M}$ is a Hermitian weight matrix. For compressible flows, Chu[73] suggests to use $\mathcal{M}$ of the form

$$\mathcal{M} = \mathcal{M}(x_\mathrm{f}, y) = \mathrm{diag}\left(\bar{\rho}, \bar{\rho}, \bar{\rho}, \frac{\bar{\rho}}{\gamma(\gamma-1)\mathrm{M}^2\,\bar{T}}, \frac{\bar{T}}{\gamma\mathrm{M}^2\bar{\rho}}\right), \tag{16}$$

where the dependency on x_f and y is inherited by using the $x_\mathrm{f}y$-dependent base-flow variables.

TABLE II. Stability analysis reference parameters representative of the most unstable 2D and 3D cases.

	c_f/u_e	$\beta\ell$	N_x	x_in/ℓ	x_out/ℓ	N_y	$y_{i,1}/\ell$	$y_{i,2}/\ell$	y_max/ℓ
#1	0.628	0	1900	0.8×10^6	2.6×10^6	160	50×10^3	—	3×10^5
#2	0.557	9.06×10^{-5}	2400	0.8×10^6	3.0×10^6	120	12×10^3	3×10^4	1×10^5
#3	0.587	9.06×10^{-5}	2400	0.8×10^6	3.0×10^6	120	12×10^3	3×10^4	1×10^5
#4	0.615	25.5×10^{-5}	2400	0.8×10^6	3.0×10^6	120	12×10^3	3×10^4	1×10^5

Based on the definition of the perturbation energy, the position of the wave packet can also be determined through the integral values

$$x_E(t_\mathrm{f}) = \frac{1}{2E}\int\int x_\mathrm{f}\, \boldsymbol{q}_\mathrm{f}'^{\mathrm{H}} \mathcal{M} \boldsymbol{q}_\mathrm{f}'\, \mathrm{d}x_\mathrm{f}\, \mathrm{d}y, \tag{17a}$$

$$y_E(t_\mathrm{f}) = \frac{1}{2E}\int\int y\, \boldsymbol{q}_\mathrm{f}'^{\mathrm{H}} \mathcal{M} \boldsymbol{q}_\mathrm{f}'\, \mathrm{d}x_\mathrm{f}\, \mathrm{d}y, \tag{17b}$$

which are the x_f- and y-coordinates of the energy centroid of the wave packet, in the fixed frame of reference. In order to determine whether a perturbation reaches the streamwise truncation boundaries, we define the streamwise extrema of the perturbations as the locations where the local perturbation energy has decayed by a factor 10^{-3} away from the maximum. Specifically, this corresponds to the upstream x_u and downstream x_d locations where the criterion

$$\frac{\int \boldsymbol{q}_\mathrm{f}'^{\mathrm{H}} \mathcal{M} \boldsymbol{q}_\mathrm{f}'\, \mathrm{d}y}{\max\limits_{x_\mathrm{f}}\left(\int \boldsymbol{q}_\mathrm{f}'^{\mathrm{H}} \mathcal{M} \boldsymbol{q}_\mathrm{f}'\, \mathrm{d}y\right)} = 10^{-3} \tag{18}$$

is satisfied.

Taking the logarithmic derivative of the energy (15) with respect to time provides (twice) the temporal growth rate of the wave-packet perturbation $\sigma(t)$. The initial perturbation energy growth rate, that is, when $t \to 0$, can be compared to the eigengrowth rate ω_i as follows:

$$\begin{aligned}\sigma(t_\mathrm{f}=0) &= \frac{1}{2E}\frac{\mathrm{d}E}{\mathrm{d}t_\mathrm{f}}(t_\mathrm{f}=0)\\ &= \underbrace{\omega_i + \frac{c_\mathrm{f}}{4E}\int\int \tilde{\boldsymbol{q}}^{\mathrm{H}} \frac{\partial \mathcal{M}}{\partial x_\mathrm{f}} \tilde{\boldsymbol{q}}\, \mathrm{d}x_\mathrm{f}\, \mathrm{d}y}_{\text{Corrected eigengrowth } \omega_{i,c}}\\ &\quad \underbrace{-\frac{c_\mathrm{f}}{4E}\int_y \tilde{\boldsymbol{q}}^{\mathrm{H}} \mathcal{M} \tilde{\boldsymbol{q}}\, \mathrm{d}y\Big|_{x_\mathrm{in}}^{x_\mathrm{out}}}_{\text{Boundary term}}.\end{aligned} \tag{19}$$

If all eigenfunctions are small at the in-/outflow boundaries, that is, if eigenfunctions are localized in the streamwise direction, the boundary term vanishes and the growth of the eigensolutions obtained in the moving frame of reference corresponds to the instantaneous growth of the perturbation in the fixed frame of reference, up to a corrective factor induced by the x dependency of the $\mathcal{M}$-matrix. Furthermore, the instantaneous velocity with which the wave packets propagate in the streamwise direction, that is, the group speed, is obtained as

$$c_\mathrm{g}(t_\mathrm{f}) = \frac{\mathrm{d}x_E}{\mathrm{d}t_\mathrm{f}}. \tag{20}$$

If the eigenfunctions corresponding to a given eigensolution are localized, then we observe that $c_\mathrm{g}(t_\mathrm{f}) \to c_\mathrm{f}$ as $t_\mathrm{f} \to 0$. We detail this further in Sec. IV B and Appendix A.

While the perturbation energy and its spatial centroid provide information regarding the global evolution of the wave packet, each single frequency constituting the wave packet can possibly be amplified differently in space and time, especially in flows that act as a selective amplifier like SWBLI.[25] Therefore, when it comes to identifying the most amplified (range of) frequencies, it is relevant to decompose the wave packet into its individual frequency components. To this end, we define the perturbation energy per individual frequency Ω_f as

$$\hat{E}(x_\mathrm{f};\Omega_\mathrm{f}) = \frac{1}{2}\int \hat{\boldsymbol{q}}(x_\mathrm{f},y;\Omega_\mathrm{f})^{\mathrm{H}} \mathcal{M}(x_\mathrm{f},y)\, \hat{\boldsymbol{q}}(x_\mathrm{f},y;\Omega_\mathrm{f})\, \mathrm{d}y, \tag{21}$$

where the variables with hats, $\hat{\boldsymbol{q}}$, correspond to the Fourier transform of the fully reconstructed perturbation variables, $\boldsymbol{q}_\mathrm{f}'$,

$$\hat{\boldsymbol{q}}(x_\mathrm{f},y;\Omega_\mathrm{f}) = \int_0^{T_s} \boldsymbol{q}_\mathrm{f}'(x_\mathrm{f},y,z=0,t_\mathrm{f})\, \mathrm{e}^{+\mathrm{i}\Omega_\mathrm{f} t_\mathrm{f}}\, \mathrm{d}t_\mathrm{f}, \quad \Omega_\mathrm{f} \in \mathbb{R} \tag{22}$$

with the sampling period T_s. The real-valued angular frequency Ω_f is introduced in order to distinguish the Fourier-transform frequency from the eigenvalues in Eqs. (12) and (14). Based on $\hat{E}(x_\mathrm{f};\Omega_\mathrm{f})$, the spatial evolution of the Fourier coefficients can be assessed by reconstructing the individual spatial amplification curves

$$\Delta N(x_\mathrm{f},\Omega_\mathrm{f}) = \frac{1}{2}\ln\frac{\hat{E}(x_\mathrm{f};\Omega_\mathrm{f})}{\hat{E}_0(x_{\mathrm{f},0};\Omega_\mathrm{f})}, \tag{23}$$

as well as the streamwise wavenumber

$$\alpha(x_\mathrm{f},\Omega_\mathrm{f}) = -\frac{\mathrm{i}}{2}\frac{\partial \ln \hat{E}(x_\mathrm{f};\Omega_\mathrm{f})}{\partial x_\mathrm{f}}, \tag{24}$$

with $x_{\mathrm{f},0}(\Omega_\mathrm{f})$ being a streamwise reference location. In order to determine the maximum amplification at each streamwise location, we then evaluate the envelope

$$\Delta N_\mathrm{max} = \max_{\Omega_\mathrm{f}}(\Delta N(x_\mathrm{f},\Omega_\mathrm{f})), \tag{25}$$

which is a useful engineering tool in the prediction of laminar–turbulent transition.

The above approach allowed us to reconstruct the traditional N-factor and neutral curves of the Blasius boundary layer (see Appendix B) and is presently considered for SWBLI in order to identify frequencies and wavenumbers related to the most amplified instability mechanisms in the shock-induced bubble.

IV. RESULTS

In what follows, the initialization of the initial-value problem (9) is discussed in Sec. IV A, the most amplified disturbance in Sec. IV B, and the underlying physical mechanisms leading to the selection of the most amplified wavelength in Sec. IV C.

A. Initial conditions: Eigensolutions

For the overarching approach to be effective, it is key to consider eigensolutions that do not depend on the truncation boundaries, that is, eigensolutions that have *both localized direct and adjoint eigenfunctions*. In this paper, an eigenfunction is deemed localized in the domain when (at least) an $\mathcal{O}(1)$-relative change in the domain length yields less than an $\mathcal{O}(10^{-4})$-relative change in both the real and imaginary parts of the eigenvalue. It is furthermore demanded that the eigenvalue converges when increasing the domain length. Based on these requirements, we identified three different types of modes. We classify these types according to their relative location with respect to the bubble apex when they achieve their maximum temporal growth rate. As depicted in Fig. 4, upstream- and downstream-type modes

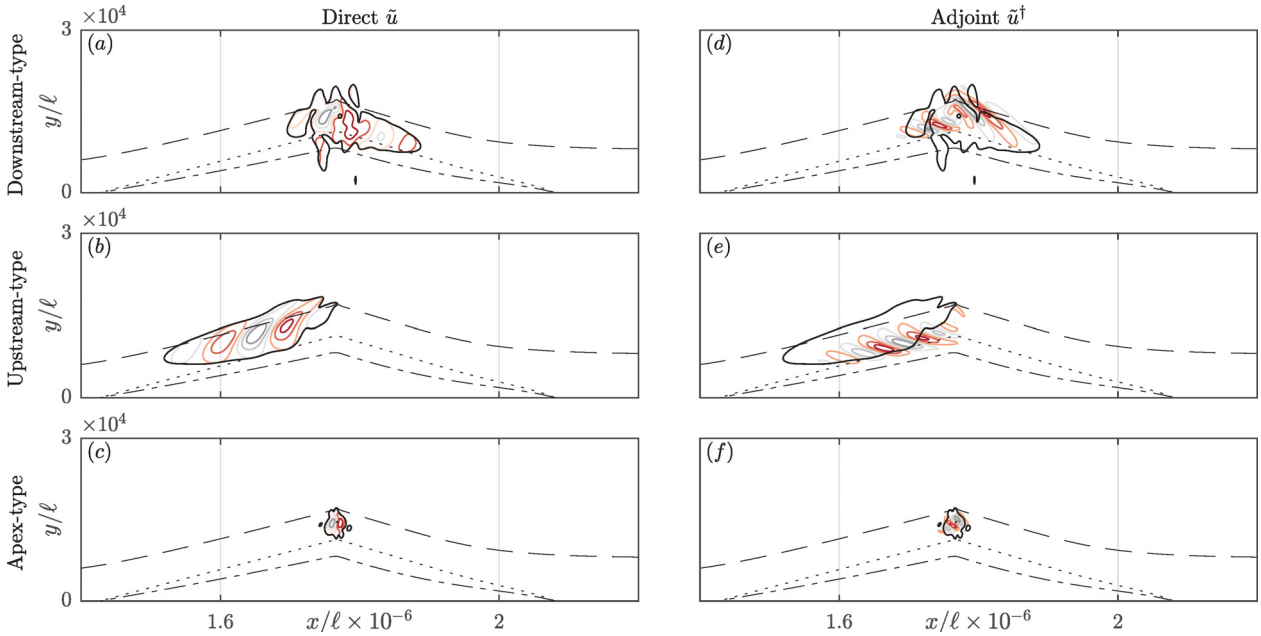

FIG. 4. Initial conditions corresponding to the most unstable eigensolution for upstream-type ($c_f/u_e = 0.557$) and downstream-type ($c_f/u_e = 0.587$) modes at β_{ud} and for apex-type mode ($c_f/u_e = 0.615$) at β_a. Colored lines from minimum (gray) to maximum (red) with $\Delta = 2/9$ for isocontours of (a)–(c) $\mathcal{R}(\tilde{u})/|\tilde{u}|_{max}$ (direct solution) and (d)–(f) $\mathcal{R}(\tilde{u}^\dagger)/|\tilde{u}^\dagger|_{max}$ (adjoint solution). (a)–(f) Isocontour of $|\tilde{u}|/|\tilde{u}|_{max}$ (solid black, level: 1/9), $\bar{U} = 0.9u_e$-isocontour (dashed black), dividing streamline (dotted black), and $\bar{U} = 0$-isocontour (dash-dotted).

were found dominant upstream and downstream of the bubble apex, respectively, while the apex-type modes are mostly dominant in the bubble-apex region. Most notably, the adjoint eigenfunctions of all observed, localized, and unstable upstream-type modes are located downstream of the direct eigenfunctions; the adjoint functions reach past the dividing streamline into the bubble. This represents an upstream-influence effect in the sense that the eigensolution is sensitive to the region occupied by the adjoint eigenfunctions, which for this case is located downstream of the direct eigenfunctions. A broad exploration of the (c_f, β)-space reveals that upstream- and downstream-type solutions reach their maximum growth rate for $\beta\ell \approx \beta_{ud}\ell = 9.06 \times 10^{-5}$ and $c_f/u_e = 0.557$ (upstream) and 0.587 (downstream), while the apex-type mode reaches its maximum growth rate at $\beta_a\ell = 25.5 \times 10^{-5}$ and $c_f/u_e = 0.615$. These values of β and c_f are used throughout the paper as reference cases in order to establish typical results obtained in the moving frame of reference (see Table II in Sec. III B for the complete set of simulation parameters alongside their definition). The spanwise wavenumbers are comparable to the findings in the literature[30,32,35] for laminar SWBLI. In particular, Dwivedi *et al.*[30] found $\beta\ell = \beta\delta_0^*/\mathrm{Re}_{\delta_0^*} = 2.6/9660 = 26.9 \times 10^{-5}$, where δ_0^* is the inlet displacement thickness, with transient growth analysis of a hypersonic SWBLI. This β-value corresponds closely to our value of $\beta_a\ell = 25.5 \times 10^{-5}$. Our frame speed also appears to be of a similar magnitude to the group speeds that are found to be relevant by Dwivedi *et al.*[30]

We carefully verified that the most unstable eigensolutions are independent of the computational setup, that is, domain size and resolution. On the one hand, at $c_f/u_e = 0.58$ and $\beta_{ud}\ell = 9.06 \times 10^{-5}$, an $\mathcal{O}(10^{-5})$-relative change in the most unstable up- and downstream-type eigenvalue is observed when displacing the domain outlet by 20%, while maintaining the same streamwise grid density, and when decreasing the streamwise resolution by 25%, for the same domain. An $\mathcal{O}(10^{-4})$-change in the most unstable upstream and downstream-type eigenvalues is observed when increasing the domain height or decreasing the wall-normal resolution by 50%. The apex-type mode is less sensitive to the domain size, as a consequence of its smaller spatial support. A 50% increase in the domain height or a 20% change in the outlet locations yields at most an $\mathcal{O}(10^{-5})$-relative change in the most unstable apex-type eigenvalue. Having shorter wavelengths in both directions, the apex-type modes are more sensitive to the grid resolution than the other modes. This is demonstrated by decreasing either the streamwise or wall-normal resolution by 25%, which induces at most an $\mathcal{O}(10^{-4})$-relative variation in the most unstable apex-type eigenvalues. In conclusion, the convergence of the solutions could be verified for all above parameters. In particular, it was observed that any $\mathcal{O}(1)$-relative change in the setup parameters yields a negligible variation in the eigensolutions. This aspect significantly improves upon the $\mathcal{O}(1)$ variation of the eigenvalues with respect to the setup parameters observed in past SWBLI studies based on a stationary-frame eigenvalue problem.

The overall eigensolution behavior upon varying the spanwise wavenumber, β, is briefly described as follows. For large enough $\beta > \beta_{ud}$, the upstream- and downstream-type modes become stable, while the apex-type mode becomes most unstable at $\beta = \beta_a$. The fact that $\beta_a > \beta_{ud}$ is not surprising due to the smaller streamwise extent of the apex-type modes. The behavior of the eigensolutions is very similar for other β-values. Hence, in this subsection, we focus on single β-values. In Sec. IV B, considering the solutions to the initial-value problem, the β-variation will be studied in more detail.

The variation of the eigensolutions with c_f yields important insight. Figure 5 illustrates the frame-speed dependency of the instantaneous growth rate and the streamwise location/extent of representative, *localized* eigenfunctions for both β_{ud} and β_a. Increasing c_f generally causes the eigenfunctions to displace upstream. This is recorded in terms of the streamwise locations x_E, x_u, and x_d of the eigenfunctions, as defined by Eqs. (17a) and (18) for $t=0$. A similar behavior is observed for the Blasius flow (Appendix A) and the cylinder wake by Kumar and Mittal.[49] The largest temporal growth rate is achieved as the eigenfunctions move past the bubble apex. For a single combination of c_f and β, several unstable eigensolutions of the same type can exist that share similar characteristics (frequency, spanwise wavenumber, spatial extent, and location). For instance, at β_{ud}, the upstream- and downstream-type families each contain three unstable, localized solutions (see Fig. 5), while only one unstable apex-type mode could be found for the present domain size. Furthermore, at β_a, Fig. 5 shows that, on the one hand, the apex-type family now contains three unstable, localized solutions and, on the other hand, no unstable upstream- and downstream-type modes could be found.

For the present flow case, no two- or three-dimensional localized eigensolutions were found when decreasing the frame speed to zero, that is, when the eigenvalue problem is solved in the stationary frame of reference. This indicates that the present SWBLI case does not support a global instability mechanism. Hence, it is necessary to consider eigensolutions for a non-zero frame speed in order to describe the pertinent instability mechanisms. More specifically, from now on, we want to consider frame speeds that yield sufficiently upstream, setup-independent eigenfunctions, so that they can be used as the initial condition for solving the initial-value problem (9) and yield converged Fourier coefficients (22) for streamwise locations of interest.

Although the apex-type mode at β_a reaches the largest eigengrowth of the entire (c_f, β)-parameter space, its very localized character in space implies that the mechanism only takes hold in a very limited spatial region around the bubble. In contrast, while the upstream- and downstream-type modes have a much smaller temporal growth rate, their effect is distributed over a much longer streamwise extent. It can be expected that these characteristics of the eigensolutions will impact their time evolution in the initial-value problem, as discussed in Sec. IV B.

B. Finite-time evolution

In the following, we determine the most amplified perturbation content, that is, spanwise wavelength and frequency, in SWBLI. The eigensolutions only reveal the largest instantaneous growth rate; their relation to the most amplified disturbance is yet to be identified. Hence, to characterize the spatial evolution of the convective instabilities, we disturb the flow with eigensolutions and assess the finite-time evolution of wave-packet perturbations by solving the initial-value problem (9) in the stationary frame of reference. In order to represent the perturbation evolution as individual-frequency amplification curves, as traditionally provided by the LST and PSE approaches, we convert the wave-*packet* signal into the monochromatic wave-*train* representation using the Fourier-transform approach detailed in Sec. III C.

First, we disturbed the flow with the apex- and upstream-type eigenfunctions at β_a and β_{ud}, respectively. The particular initial

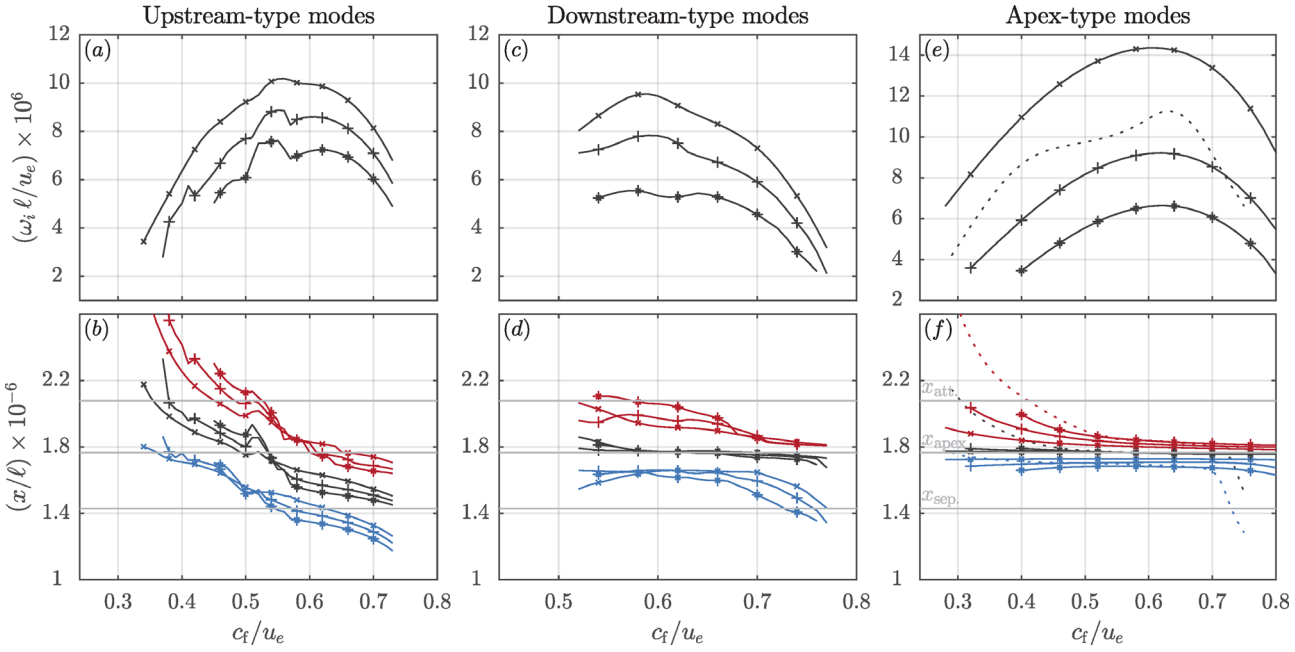

FIG. 5. Variation of the initial-condition characteristics ($t=0$ only) with respect to the frame speed c_f. (a) and (b) Upstream-, (c) and (d) downstream-, and (e) and (f) apex-type modes for $\beta_{ud}\ell = 9.06 \times 10^{-5}$ (a)–(d) and $\beta_a\ell = 25.5 \times 10^{-5}$ (e)–(f). Crosses, pluses, and stars rank modes from most unstable to third-most unstable. Dotted line for unique apex-type mode at β_{ud}. (a), (c), and (e) Temporal growth rate ω_i and (b), (d), and (f) streamwise energy centroid x_E (black), upstream x_u (blue), and downstream x_d (red) extrema of the eigenfunctions. (b), (d), and (f) Gray lines indicate streamwise coordinates of separation ($x_{sep.}$), bubble apex (x_{apex}), and reattachment ($x_{att.}$).

conditions are chosen based on the β-values maximizing the instantaneous growth rate (for all β- and c_f-values). Later, we will study the effect of varying β while using both initial conditions. Since amplification curves over the largest streamwise extent of the shock-induced bubble are sought, we use the most upstream initial condition, per mode type, in order to obtain converged Fourier coefficients in the region of interest. The highest frame speed for which localized solutions are found is $c_f = 0.73u_e$. Note that the initial condition must be localized in space to ensure that the resulting temporal solution is not a boundary-dependent wave-train solution but is instead a wave packet containing a broad range of frequencies. All the solutions considered to initialize the temporal problem are independent of the numerical setup. Using these initial conditions, we verify Eq. (19) for small elapsed times in the sense that the corrected eigengrowth rate $\omega_{i,c}$ and the instantaneous energy growth rate $\sigma(t_f)$ are equal up to $O(10^{-6})$ and $O(10^{-5})$ relative errors for upstream- and apex-type modes, respectively. A similar result holds when comparing the instantaneous group speed $c_g(t_f)$ against the frame speed c_f. In this framework, eigensolutions are thus demonstrated to be representative of the instantaneous perturbation dynamics. For longer-time dynamics, the Fourier coefficients of the time-evolved wave packets are computed and are presented in Fig. 6(a). All curves are normalized at $x_{f,0}/\ell = x_{apex}/\ell = 1.77 \times 10^6$, which corresponds to the most upstream location where converged Fourier coefficients can be found for the *apex*-type modes since no eigenfunction of this mode type can be found far upstream of the bubble apex.

The Fourier coefficients in Fig. 6(a) show that, although the apex-type modes have the largest growth rate around the incident shock, they do not yield the largest amplification-factor envelope over the extent of the bubble. This behavior was expected from the apex-type eigensolutions shown in Fig. 5: the large growth rate is achieved only over a very small streamwise extent of the bubble. In contrast, the upstream-type wave packet at β_{ud} covers a much longer extent of the shock-induced bubble in the streamwise direction and, despite a relatively smaller growth rate as suggested by the eigensolutions, yields the largest spatial amplification in the SWBLI. Following this reasoning, downstream-type modes can only cover a shorter streamwise extent of the bubble than that of upstream modes. Since their corresponding temporal growth rate is smaller than or equal to that of upstream-type modes, downstream-type modes could only reveal a smaller overall amplification and thus are omitted for sake of conciseness.

A parametric study on the spanwise wavenumber is performed in order to identify the critical β-values yielding the largest perturbation amplification. We cover β/β_{ud}-values over the range from 0 to 1.5 for the upstream-type mode and β/β_a-values from 0.25 to 1.5 for the apex-type mode, both with uniform steps of 0.25. The frame speed used to obtain the initial conditions is kept at $c_f = 0.73u_e$ for all cases. The resulting amplification envelopes are given in Fig. 6(b) for upstream-type (solid) and apex-type (dashed) modes. These results indicate that, for the present SWBLI conditions, the most critical three-dimensional convective instabilities are characterized by a spanwise wavelength $\lambda_z/\ell \approx 2\pi/(\beta_{ud}\ell) = 6.9 \times 10^4$, which is approximately 10.7 times smaller than the length of the bubble ($L_{sep}/\ell \approx 6.5 \times 10^5$), and a frequency of about $f = 9.3(\pm 0.58)$ kHz at the reattachment point. Due to the present selection of discrete β-values used for the parametric study, the uncertainty on the most-amplified spanwise wavenumber reasonably scales to about $\pm 2.7\%$ of the bubble length.

Considering the bubble length as a reference length, the characteristic frequency of the present convective mechanisms corresponds to a Strouhal number $\mathrm{St} = fL_{sep}/u_e = 0.38$ that is in the medium-frequency range ($\mathrm{St} = 0.3 - 0.5$) of the frequencies that can be found in SWBLIs.[25,26,31–33,38,74] While Bonne *et al.*[31] associated these medium frequencies with large-scale breathing motions of the bubble in transitional SWBLIs, Sasaki *et al.*,[28] Nichols *et al.*[33] (turbulent), and Bugeat *et al.*[32] (laminar) suggest instead that medium frequencies represent convective instability mechanisms of the shear-layer and that the bubble breathing occurs in the low-frequency range ($\mathrm{St} < 0.1$). In this range, the breathing motion would be associated with a low-frequency global mode encompassing the entire recirculation region.[32,33,35] Since

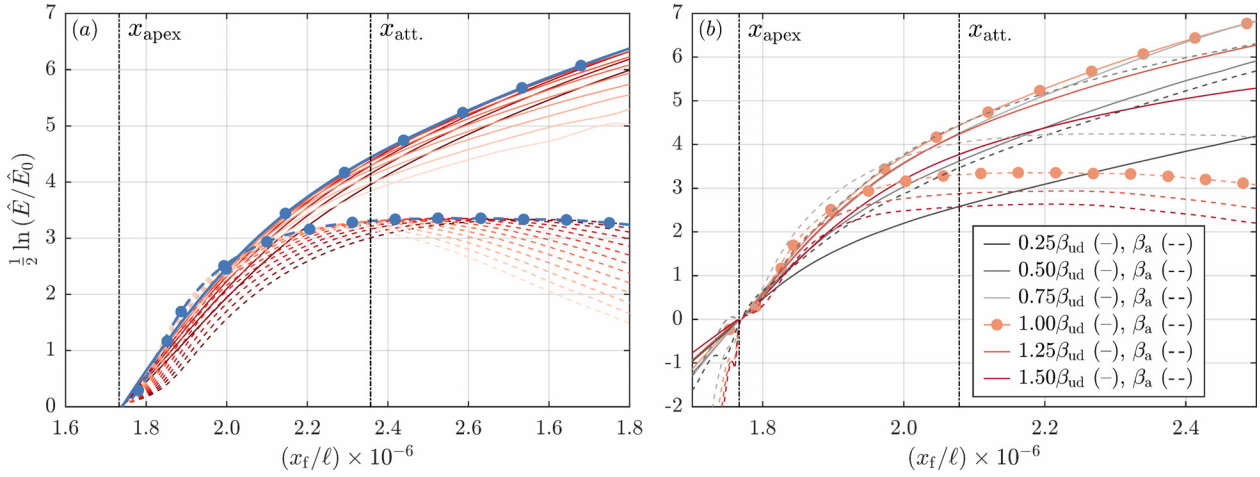

FIG. 6. (a) Amplification curves and (b) envelope of amplification factor curves normalized at $x_{f,0}/\ell = 1.77 \times 10^6$. (a) Apex mode at β_a (dashed) and upstream mode at β_{ud} (solid) for frequencies $\Omega_r\ell/u_e \times 10^5$ ranging from 2.077 (light red) to 4.845 (dark red) with step 0.23. Envelopes of individual amplification curves indicated by blue lines and filled circles. (b) Envelope for upstream- (solid) and apex-type (dashed) modes at different β (colored lines). Filled circles for envelopes at β_{ud} and β_a of panel (*a*). Vertical dash-dotted lines: streamwise location of the bubble apex and reattachment.

the wave packets observed in our flow configuration are dominant in the shear layer, we expect that the present linear convective mechanisms cannot be representative of a self-sustained large-scale breathing of the bubble.

The β-parameter study reveals that the spanwise wavenumber $\beta = \beta_{ud}$ yields the largest amplification when using the upstream-type initial condition. Remarkably, it also maximizes the amplification of the apex-type initial condition, as observed for the case with the β-value closest to β_{ud}, that is, $\beta = 0.5\beta_a \approx \beta_{ud}$. Hence, although β_a yields the maximum growth rate of the apex-type mode, it does not lead to the maximum amplification. The solutions initialized with the upstream- and apex-type modes with $\beta \approx \beta_{ud}$ are found to display similar characteristics. For example, we observe that the most amplified frequency at the reattachment point is similar (9.3 ± 0.58 kHz) and, also that the mechanisms underlying the growth are very similar (this is quantified in Fig. 8, presented in Sec. IV C). This shows that the most amplified disturbance can be identified with more than one type of initial condition and thus that β_{ud} effectively yields the largest amplification. Note that disturbing the flow with the upstream-type solutions is preferred over downstream- or apex-type modes in the sense that the region of converged Fourier coefficients reaches farther upstream of the shock-induced bubble and spans a much larger streamwise extent of the perturbation growth in the flow.

To further ensure that the most critical dynamics are effectively captured by one initial condition, we performed a sensitivity study by disturbing the flow with, on the one hand, upstream-type eigenfunctions obtained at $c_f/u_e = 0.67$, 0.70, and 0.73, and, on the other hand, the three most unstable solutions of the upstream-type family at $c_f/u_e = 0.73$. The amplification curves are shown in Fig. 7 at three different frequencies and are indistinguishable from one initial condition to another. The only difference is observed in the spatial extent of the region within which converged Fourier coefficients could be obtained; the more upstream the initial condition, the longer the spatial extent. Hence, when using the present methodology, we advise considering the most upstream and localized initial condition by means of changing (usually increasing) the frame speed. Since amplification curves are independent of the frame speed and eigenfunctions, a single localized initial condition is sufficient to reveal the most-amplified perturbation dynamics.

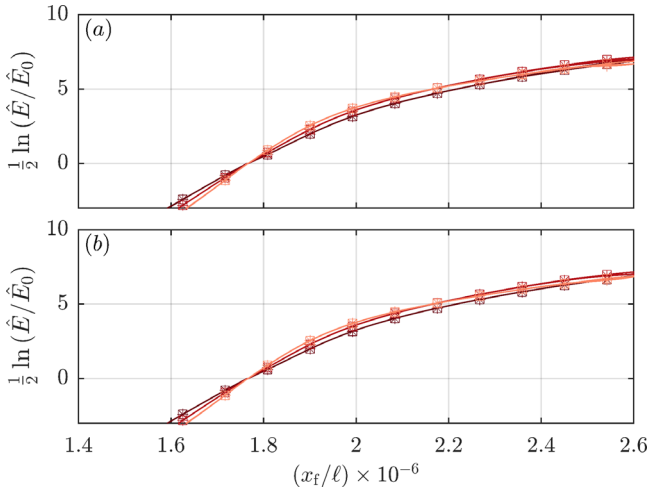

FIG. 7. Spatial amplification of upstream-type wave packets for $\beta = \beta_{ud}$. Individual-frequency amplification curves obtained from initialization with (a) the three most unstable eigenfunctions of the upstream-type family (from most unstable to least unstable: squares, crosses, and pluses) at $c_f/u_e = 0.73$ and (b) the most unstable eigenfunction at $c_f/u_e = 0.67$ (pluses), 0.70 (crosses), and 0.73 (squares). Colored lines for frequencies $\Omega_f \ell/u_e \times 10^5 = 0.2307$, 0.3461, and 0.3922 (light to dark red).

In order to be effective, the present method requires using initial conditions that are located upstream of the region where perturbation growth is expected. Although the complexity in meeting this requirement depends on the flow configuration, we argue that this is the main limitation of our approach. In the present study, it is possible to find such upstream solutions, but it may be more difficult, if not impossible, in other cases (SWBLIs or much broader classes of flows). We find that the eigenfunctions rapidly move into the upstream boundary layer as we increase the frame speed to large enough values while fixing all other parameters. It is very difficult to track and appropriately spatially resolve the eigenfunctions whenever this happens (with a grid focused on the interaction region), because the streamwise extent of the eigenfunctions increases immensely upstream with a small increase in the frame speed. As a solution, we recommend using the wave-packet tracking strategy described by Browne *et al.*[75] to provide increased flexibility in tracking the eigenfunctions as β and c_f, or other parameters, are varied.

C. Physical mechanisms

The mechanisms that contribute to the three-dimensional instabilities are discussed after decomposing the temporal growth rate into its different contributions. To do this, we factor the temporal growth $\sigma(t)$, as defined in Eq. (19), from the wave-packet perturbation $\boldsymbol{q}'_f(x,y,t)$, such that $\boldsymbol{q}'_f(x,y,t) = \breve{\boldsymbol{q}}(x,y,t)e^{\sigma(t)t}$ at each time instant and then use the Reynolds–Orr decomposition[76] based on Chu's norm [see Eq. (16)] for the measurement of the perturbation energy.[77] Among the many terms of the perturbation equations, only a few have a significant contribution to the energy growth. A careful inspection, that included all terms, showed that terms contributing more than 5% to the temporal growth rate dictate its overall trends across all considered cases. Hence, we focus the present analyses on those terms. All other terms individually contributing less than 5% to the energy growth are included in a remainder that itself, that is, the sum of the neglected terms, represents less than 10% of the growth rate. Hence, the decomposition of the growth rate can be written as

$$\sigma = \underbrace{R_{\breve{u}^*\breve{v}} + R_{|\breve{u}|^2}}_{\text{Reynolds stresses}} + \underbrace{R_{\breve{s}^*\breve{v}} + R_{\breve{s}^*\breve{u}}}_{\text{Reynolds heat fluxes}} + \underbrace{D_{\breve{u}} + D_{\breve{w}} + D_{\breve{T}}}_{\text{Dissipation}} + \text{remainder} \tag{26}$$

with

$$R_{\breve{u}^*\breve{v}} = -\mathcal{R}\left\{\int\int \breve{u}^*\breve{v}\,\bar{\rho}\,\frac{\partial \bar{U}}{\partial y}\frac{dx\,dy}{E}\right\}, \tag{27a}$$

$$R_{|\breve{u}|^2} = -\mathcal{R}\left\{\int\int |\breve{u}|^2\bar{\rho}\,\frac{\partial \bar{U}}{\partial x}\frac{dx\,dy}{E}\right\}, \tag{27b}$$

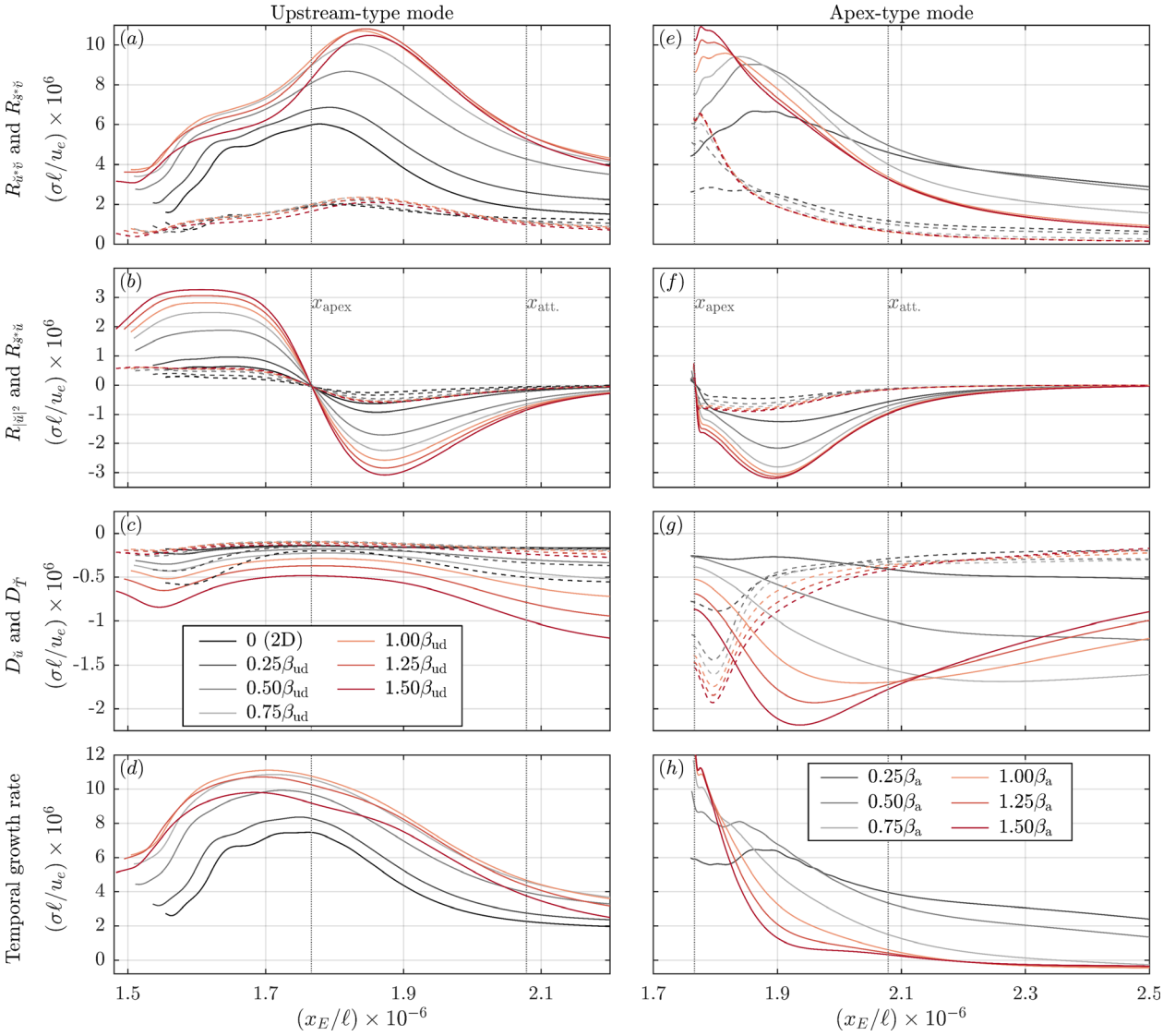

FIG. 8. Streamwise variation of the dominant contributions to the temporal growth rate [Eq. (26)] of the temporal wave packets: (a) and (e) $R_{\breve{u}^*\breve{v}}$ (solid) and $R_{\breve{s}^*\breve{v}}$ (dashed), (b) and (f) $R_{|\breve{u}|^2}$ (solid) and $R_{\breve{s}^*\breve{u}}$ (dashed), (c) and (g) $D_{\breve{u}}$ (solid) and $D_{\breve{T}}$ (dashed), and (d) and (h) temporal growth rate $\sigma(t)$. (a)–(d) Upstream- and (e)–(h) apex-type modes for relevant β-values. (a)–(h) Vertical dotted lines: streamwise location of the bubble apex and reattachment.

$$R_{\breve{s}^*\breve{v}} = -\mathcal{R}\left\{\iint \breve{s}^*\breve{v}\,\bar{\rho}\,\frac{\partial \bar{T}}{\partial y}\frac{\mathrm{d}x\,\mathrm{d}y}{E}\right\}, \tag{27c}$$

$$R_{\breve{s}^*\breve{u}} = -\mathcal{R}\left\{\iint \breve{s}^*\breve{u}\,\bar{\rho}\,\frac{\partial \bar{T}}{\partial x}\frac{\mathrm{d}x\,\mathrm{d}y}{E}\right\}, \tag{27d}$$

$$D_{\breve{u}} = \frac{1}{\mathrm{Re}}\mathcal{R}\left\{\iint \bar{\mu}\breve{u}^*\frac{\partial^2 \breve{u}}{\partial y^2}\frac{\mathrm{d}x\,\mathrm{d}y}{E}\right\}, \tag{27e}$$

$$D_{\breve{w}} = \frac{1}{\mathrm{Re}}\mathcal{R}\left\{\iint \bar{\mu}\breve{w}^*\frac{\partial^2 \breve{w}}{\partial y^2}\frac{\mathrm{d}x\,\mathrm{d}y}{E}\right\}, \tag{27f}$$

$$D_{\breve{T}} = \frac{1}{\mathrm{Ec\,Re\,Pr}}\mathcal{R}\left\{\iint \frac{\bar{\kappa}}{\bar{T}}\breve{T}^*\frac{\partial^2 \breve{T}}{\partial y^2}\frac{\mathrm{d}x\,\mathrm{d}y}{E}\right\}. \tag{27g}$$

In the above expressions, $\breve{\boldsymbol{q}} = [\breve{u}\,,\breve{v}\,,\breve{w}\,,\breve{T}\,,\breve{\rho}\,]^{\mathrm{T}}$, $\mathcal{R}\{\cdot\}$ denotes the real part, and the specific disturbance entropy, $\breve{s}$, is defined as

$$\gamma \mathrm{M}^2 \breve{s} = \frac{\gamma}{\gamma-1}\frac{\breve{T}}{\bar{T}} - \frac{\breve{p}}{\bar{P}} = \frac{1}{\gamma-1}\frac{\breve{T}}{\bar{T}} - \frac{\breve{\rho}}{\bar{\rho}}. \tag{28}$$

We verified that obtaining σ from the energy budget, Eq. (26), or from the temporal derivative of the perturbation energy, Eq. (19), is equivalent up to machine precision.

With the decomposition of the growth rate given by Eq. (26), we can distinguish several growth mechanisms of different nature. First, the production terms induced by the Reynolds-stress (Reynolds-heat-flux), denoted by R, produce a streamwise velocity (entropy) perturbation through the effect of wall-normal advection of the base-flow velocity (temperature) by the wall-normal velocity perturbations. Since the perturbations are mostly confined in the shear-layer, which has a much smaller characteristic length scale in the wall-normal direction than in the streamwise direction, the quantities involving the wall-normal derivatives are, even in this arguably strongly two-dimensional flow field, much larger than the streamwise-derivative terms. Hence, the Reynolds-stress $R_{\breve{u}^*\breve{v}}$ and heat-flux $R_{\breve{s}^*\breve{v}}$ terms that involve the wall-normal derivative of the base-flow quantities likely prevail over the terms involving the derivative in the other direction. Since these wall-normal Reynolds-stress and heat-flux terms originate in the linearization of the advection term of the Navier–Stokes equations, they involve the wall-normal velocity perturbation component, which could be interpreted as moving the base-flow quantities (infinitesimally) upward away from the wall or downward to the wall. Second, the energy growth can be attenuated through the dissipation of the velocity or temperature perturbations. The responsible terms are indicated by D. Although the dissipation of perturbations is governed by a significant number of terms (see the ω_i-decomposition of Padilla Montero and Pinna[77]), Eqs. (27e)–(27g) are truncated to only keep the terms that are at least 5% of ω_i, per perturbation component. For all components, these terms correspond to second derivatives in the wall-normal direction. The significant terms of Eq. (27) are computed along $x_E(t)$ of the temporally evolving wave packets and are shown in Fig. 8; panels 8(a), 8(b), 8(c), and 8(d) show the results for the upstream-type mode and 8(e), 8(f), 8(g), and 8(h) for the apex-type mode.

As a consequence of the large wall-normal gradient $\partial\bar{U}/\partial y > 0$ and the substantial region where $\breve{u}$ and $\breve{v}$ are out-of-phase (i.e., $\mathcal{R}\{\breve{u}^*\breve{v}\} < 0$), the Reynolds stress $R_{\breve{u}^*\breve{v}}$ is the largest contribution to

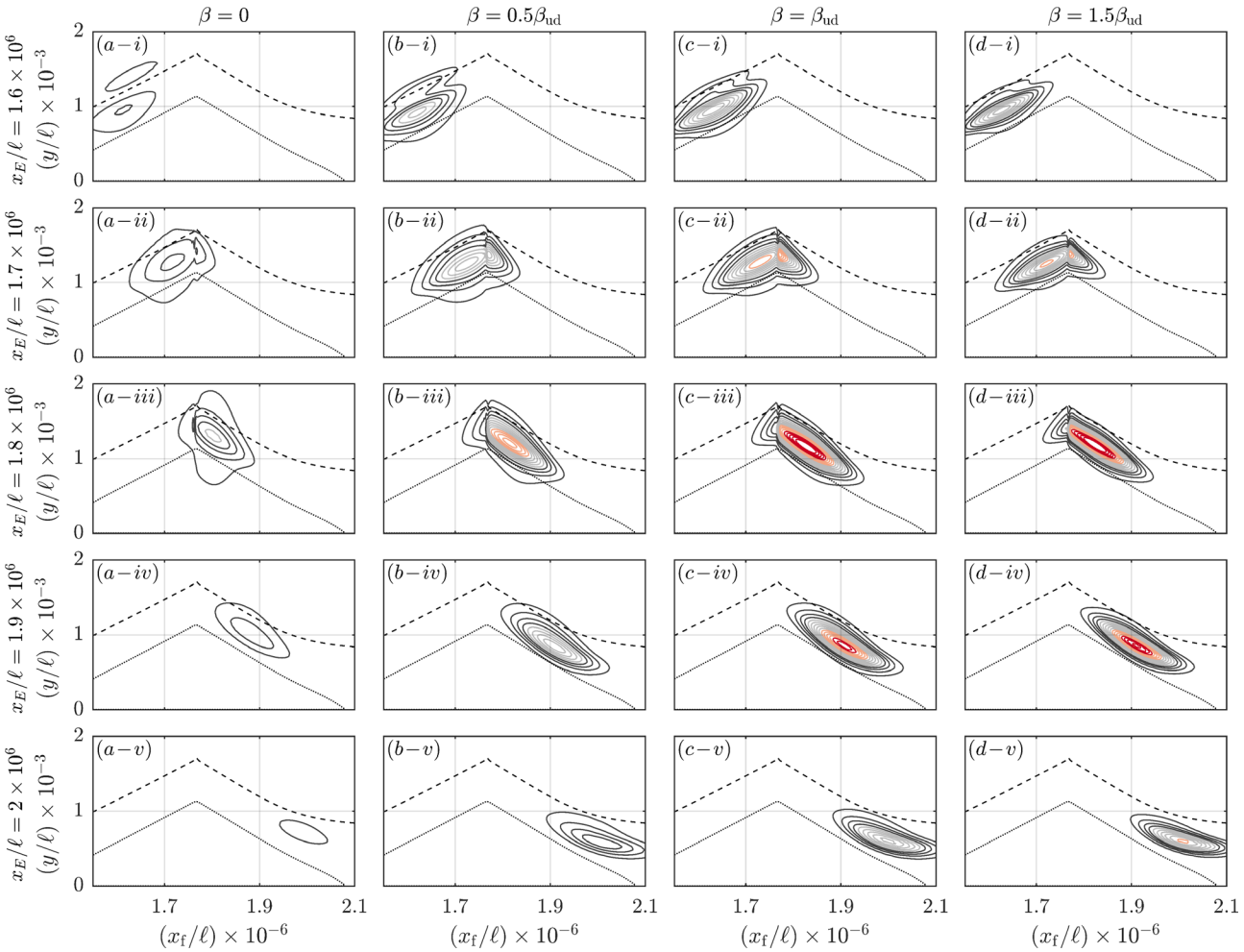

FIG. 9. Wall-normal Reynolds stress for different β [columns (a)–(d)] at several locations of the x-centroid [rows (i)-(v)] of the upstream-type wave packet. Isocontours of $\mathcal{R}\{\breve{u}^*\breve{v}/E\} \times \rho_e\ell^2$ indicated by colored lines from -9×10^{-10} (red) to -0.5×10^{-10} (gray) with $\Delta = 0.5 \times 10^{-10}$. Boundary-layer edge ($\delta_{90}$, dashed) and dividing streamline (dotted).

the growth rate, for both the upstream- and apex-type wave packets. Furthermore, $R_{\breve{u}^*\breve{v}}$ is strongly activated in the region of the bubble apex as the wave packets move downstream such that it reaches its largest destabilizing contribution downstream of the bubble apex, in close vicinity of the incident shock. In this region, the factor $\bar{\rho}\partial\bar{U}/\partial y > 0$ is relatively constant in the streamwise direction. Consequently, as shown in Fig. 9, the large size of $R_{\breve{u}^*\breve{v}}$ in the apex region is caused by a significant growth of $\mathcal{R}\{\breve{u}^*\breve{v}/E\}$ downstream of the shock.

A similar behavior is observed for the Reynolds heat-flux $R_{\breve{s}^*\breve{v}}$. For the upstream-type wave packets, however, the contribution of $R_{\breve{s}^*\breve{v}}$ is an order of magnitude smaller than that of $R_{\breve{u}^*\breve{v}}$. This follows from: (1) the smaller wall-normal gradient $\partial\bar{T}/\partial y$, (2) the reduced unbalance between the out-of-phase and in-phase regions of $\breve{s}$ and $\breve{v}$, and (3) the smaller relative size of $\breve{T}$ compared to $\breve{u}$. These last two effects are, nonetheless, mitigated for apex-type wave packets such that $R_{\breve{s}^*\breve{v}}$ and $R_{\breve{u}^*\breve{v}}$ together produce most of the perturbation energy, especially in the immediate vicinity of the bubble apex.

Depending on the wave-packet location in the bubble, the streamwise Reynolds-stress $R_{|\breve{u}|^2}$ and Reynolds-heat-flux $R_{\breve{s}^*\breve{u}}$ terms contribute to producing or destroying perturbation energy. The positive or negative contribution of these terms is set by the streamwise gradient of the streamwise base-flow velocity, $\partial\bar{U}/\partial x$, that has opposite signs on the two sides of the bubble. Hence, when the incoming perturbation crosses the bubble apex, $R_{|\breve{u}|^2}$ and $R_{\breve{s}^*\breve{u}}$ rapidly become stabilizing as the flow accelerates and eventually reach their maximum stabilizing contribution in the aft-bubble region. $R_{|\breve{u}|^2}$ becomes as large as 30% of $R_{\breve{u}^*\breve{v}}$ in absolute value. Thereby, $R_{|\breve{u}|^2}$ prevents the maximum temporal growth to occur in the post-shock region [see Fig. 8(g)]. Instead, the temporal growth rate is maximum upstream of the apex when $R_{|\breve{u}|^2}$ produces perturbation energy along $R_{\breve{u}^*\breve{v}}$. Hence, while the Reynolds stress $R_{\breve{u}^*\breve{v}}$ term is usually the largest contribution to the growth rate in wall-bounded flows, we observe that $R_{|\breve{u}|^2}$ plays a significant role in the present flow configuration in which the streamwise velocity rapidly varies in the streamwise direction.

The contribution of the streamwise Reynolds-stress $R_{|\breve{u}|^2}$ to the perturbation energy becomes more significant as β increases. This is further supported by the Pearson correlation coefficient, when comparing the streamwise variation of $R_{\breve{u}^*\breve{v}}$ with the temporal growth rate. This coefficient decreases from 0.99 ($\beta = 0$) to 0.82 ($\beta = 1.5\beta_{\mathrm{ud}}$), for the upstream-type wave packet, while the correlation between $R_{\breve{u}^*\breve{v}} + R_{|\breve{u}|^2}$ and the temporal growth rate remains constant. For the apex-type wave packet, slightly weaker correlations are found, except when additionally including the wall-normal Reynolds-heat-flux term that produces significant perturbation energy alongside $R_{\breve{u}^*\breve{v}}$.

The dissipation terms for the upstream- and apex-type modes are shown in Figs. 8(e) and 8(f), respectively. These terms present one of the main differences between the aforementioned mode types, which is explained by their high correlation with both the spatial extent and wavenumber of the wave packet. Hence, the dissipation terms of the apex-type wave packets, that have a short streamwise extent and wavelength, are much stronger than that of upstream-type wave packets. Furthermore, since the amplitude of $\breve{T}$ and $\breve{u}$ are similar for the apex-type mode, $D_{\breve{T}}$ and $D_{\breve{u}}$ dissipate a similar amount of perturbation energy. In contrast, upstream-type wave packets have a much larger ratio $|\breve{u}|/|\breve{T}|$, especially for increasing β, and are thus mostly stabilized by $D_{\breve{u}}$.

The Reynolds stress $R_{\breve{u}^*\breve{v}}$ and heat-flux $R_{\breve{s}^*\breve{v}}$ are both maximized over the span of the shock-induced bubble at β_{ud}, which also maximizes the amplification envelope. This can be explained by considering the evolution of $\mathcal{R}\{\breve{u}^*\breve{v}/E\}$ as depicted in Fig. 9. For an increasing spanwise wavenumber, we observe that $\mathcal{R}\{\breve{u}^*\breve{v}/E\}$ increases in magnitude and, simultaneously, covers a smaller area in space. These two variations have an antagonistic effect on the integral value $R_{\breve{u}^*\breve{v}}$ that thus attains a maximum for $\beta = \beta_{\mathrm{ud}}$. The Reynolds heat-flux $R_{\breve{s}^*\breve{v}}$ features a similar behavior, but to a lesser extent following both its smaller magnitude and weaker dependency on β than that of $R_{\breve{u}^*\breve{v}}$. Accordingly, we conclude that the wall-normal Reynolds stress $R_{\breve{u}^*\breve{v}}$, being the most destabilizing contribution, arguably governs the amplification of convective perturbations across the SWBLI.

V. CONCLUSION

In the present paper, we performed linear stability analysis of a laminar SWBLI to determine the most amplified convective disturbance mechanisms. The laminar SWBLI base-flow field was obtained by using the selective frequency damping approach, which, prior to linear stability analyses, reveals that the flow does not support the temporal growth of a disturbance in a fixed region of space. This means that no two-dimensional global instabilities exist in the present configuration and, thus, at least all two-dimensional instability mechanisms should be convective. Furthermore, as part of the linear stability analyses, no three-dimensional global modes were found. Since no eigensolutions that are localized in the streamwise direction could be found in the *stationary* frame of reference, an alternative approach that can represent convective instability mechanisms is considered. According to the presence of large gradients in the base flow, we devised our approach to appropriately account for all elliptical effects in the streamwise-wall-normal plane in order to represent any feedback mechanism that could be supported in the region of reverse flow. To satisfy these criteria, the proposed methodology consists in solving the initial-value problem for the linear perturbations while using special initial conditions that are eigenfunctions obtained in a *moving* frame of reference.

In the moving frame, convective mechanisms are captured as eigensolutions with eigenfunctions that are localized in the streamwise direction; thereby, the solutions are independent of the computational setup (truncation-boundary positions and conditions and grid resolution). For the present flow, we identified three types of unstable, localized modes (upstream-, downstream-, or apex-type modes) for a wide range of spanwise wavenumbers and frame speeds. The characteristic frequency of these instability mechanisms is at least one order of magnitude larger than what is usually observed for the low-frequency breathing of the bubble and none of the linear mechanisms found could be related to any low-frequency unsteadiness of the SWBLI. Instead, the medium-frequency mechanisms that are presently found represent convective instability mechanisms of the separated shear layer and can enter the reverse-flow region.

By considering the finite-time evolution of the wave-packet perturbations obtained from the initial-value problem using the moving-frame eigenfunctions as initial condition, we assess the spatial evolution of the convective instabilities. First, we quantify the perturbation amplification by reconstructing the individual-frequency amplification curves by Fourier transforming the signal. To the greatest extent, this allows us to determine the most amplified perturbation content of SWBLI, in particular in terms of the most amplified spanwise

wavelength, which is found to be as large as about 10% of the bubble length, and frequency, which is about 9 kHz at the streamwise location of the reattachment. Second, we decompose the perturbation wave-packet into the individual components that contribute to its growth. We observe that the wall-normal Reynolds stress produces most of the disturbance energy over the whole extent of the SWBLI. Nevertheless, we find that, although the streamwise Reynolds stress has a smaller magnitude, it can interfere either productively or destructively with the wall-normal Reynolds stress depending on whether the wave-packet is located upstream or downstream of the bubble apex. This contribution of the streamwise Reynolds-stress results in an overall upstream shift of the maximum temporal growth and intensifies when increasing the spanwise wavenumber β. Finally, at a particular spanwise wavenumber $\beta = \beta_{ud}$, the (integral) wall-normal Reynolds-stress and Reynolds-heat flux of the temporal wave-packet are maximized along the complete spatial extent of the shock-induced bubble. By analyzing the variation of the spatial organization of the dominant factors that appear in the integrand of the wall-normal Reynolds-stress term as β increases, we find that its maximum magnitude increases, while the area over which it is active shrinks so that it leads the integral value to reach a maximum for $\beta = \beta_{ud}$. In turn, the largest amplification in the present flow configuration is achieved for this wavenumber, which also corresponds to the spanwise wavenumber that displays the maximum growth rate of the moving-frame initial condition.

We argue that the solutions of the eigenvalue problem solved in a moving frame of reference are remarkably convenient to initialize the perturbation problem for several reasons. First, the eigensolutions in the moving frame are independent of the computational setup (truncation-boundary positions and conditions and grid resolution). Second, the eigensolutions indicate the main characteristics (wavelength and frequency) of the instability mechanisms in an instantaneous sense, ahead of solving the (initial-value) perturbation problem. When disturbing the flow with the moving-frame solutions to obtain the finite-time behavior of the instabilities, we show that the initial, short-time perturbation dynamics coincide with the dynamics predicted by the moving-frame eigensolutions. Hence, the time response of the flow to these initial conditions is not polluted by any inadvertent transient behavior. Third, the temporal evolution of the resulting wave packets is independent of the frame speed and the mode chosen to initialize the problem. This aspect is even more remarkable considering that the dynamics of the most amplified wave packet are independent of whether an upstream- or apex-type eigensolution is used as the initial condition to disturb the flow.

In conclusion, we demonstrated that using moving-frame eigenfunctions as initial conditions of the perturbation problem allows the elliptic representation of two-dimensional convective instabilities without being limited by solutions that are dependent on the numerical setup. In practice, this methodology allows us to characterize the most amplified instabilities in the SWBLI. The adjoint eigensolutions and adjoint initial-value problem can be used, in future studies, as a means to study how the disturbances that are inherent to the separation bubble are effectively forced (far) upstream of the bubble. An adjoint solution moving out of the boundary layer and toward the freestream, for example, would indicate that the inherent disturbances are sensitive to freestream turbulence and insensitive to forcing at the wall. Finally, we emphasize that the present study reveals the linear mechanisms yielding strong amplification of perturbations in a short streamwise extent of the flow.

Without having applied our approach to other flow configurations, we believe that it paves the way for the structured characterization of the laminar–turbulent transition of separation bubbles in general (including the incompressible, transonic, and hypersonic regimes), starting from the homogeneous, linear, convectively unstable disturbance mechanisms. It is likely that separation bubbles will show similar, more, or fewer mode types and that modes other than the upstream-type mode can dominate in particular conditions. Future research efforts should be invested in thoroughly exploring the behavior of the newly found mechanisms for other flow configurations (varying Mach number, Reynolds number, shock strength, etc.).

The present work proposes an insight into primary convective instabilities in SWBLI through linear stability analyses and, at this stage, we do not consider nonlinear effects that would take place when the perturbation amplitude becomes significantly large. Assessing nonlinear mechanisms, however, requires a judicious choice of initial conditions. By using the moving-frame solutions, our approach offers a careful control of these initial conditions and, thus, provides a structured strategy that can be applied to study the route from linear perturbation growth to laminar–turbulent transition in SWBLI.

ACKNOWLEDGMENTS

The authors acknowledge the funding provided to Sébastien E.M. Niessen by the Fonds National de la Recherche Scientifique de Belgique (F.R.S.-FNRS) under Grant No. FC27285 and the computational resources provided by the Consortium des Équipements de Calcul Intensif (CÉCI), funded by the F.R.S.-FNRS under Grant No. 2.5020.11 and by the Walloon Region (Belgium).

AUTHOR DECLARATIONS

Conflict of Interest

The authors have no conflicts to disclose.

Author Contributions

Sébastien E. M. Niessen: Conceptualization (equal); Data curation (equal); Formal analysis (equal); Funding acquisition (equal); Investigation (equal); Methodology (equal); Software (equal); Validation (equal); Visualization (equal); Writing – original draft (equal); Writing – review & editing (equal). **Koen Jasper Groot:** Conceptualization (equal); Formal analysis (equal); Investigation (equal); Methodology (equal); Supervision (lead); Visualization (equal); Writing – original draft (supporting); Writing – review & editing (lead). **Stefan Hickel:** Conceptualization (equal); Methodology (equal); Software (equal); Supervision (equal); Writing – review & editing (equal). **Vincent E. Terrapon:** Funding acquisition (equal); Methodology (equal); Supervision (equal); Writing – review & editing (equal).

DATA AVAILABILITY

Raw data were partly generated by the computational resources provided by the Consortium des Équipements de Calcul Intensif (Belgium). Derived data supporting the findings of this study are available from the corresponding author upon reasonable request.

APPENDIX A: INITIAL CONDITIONS AND SHORT-TIME WAVE-PACKET EVOLUTION IN THE BLASIUS BOUNDARY LAYER

In the following, we use the moving-frame approach to obtain stability results for the Blasius boundary layer, which can be reproduced up to machine precision. By conducting stability analyses in moving frames, we find that it is possible to obtain eigensolution families with localized eigenfunctions for a range of frame speeds; the largest ω_i-value was obtained for $c_f/u_e = 0.415 \pm 0.005$. The corresponding direct and adjoint eigenfunctions are shown in Fig. 10. Since the eigenfunctions are localized in the domain, the overall eigensolutions are negligibly impacted by the numerical setup, as illustrated in Table III for the first and fifth most unstable modes at $c_f/u_e = 0.415$.

We can assess the impact of the frame speed on the eigensolutions by measuring the streamwise characteristics of the eigenfunctions (streamwise wavelength, centroid location, and up-/downstream extrema) with respect to the frame speed. In particular, Fig. 11 shows that reducing the frame speed increases the streamwise span of the eigenfunctions. Remarkably, this evolution occurs at a higher rate than the rate at which the streamwise wavelength varies with the frame speed. Obtaining setup-independent eigensolutions (i.e., solutions with localized eigenfunctions) for lower frame speeds thus requires increasing both the domain length and the amount of streamwise grid points. A direct consequence is

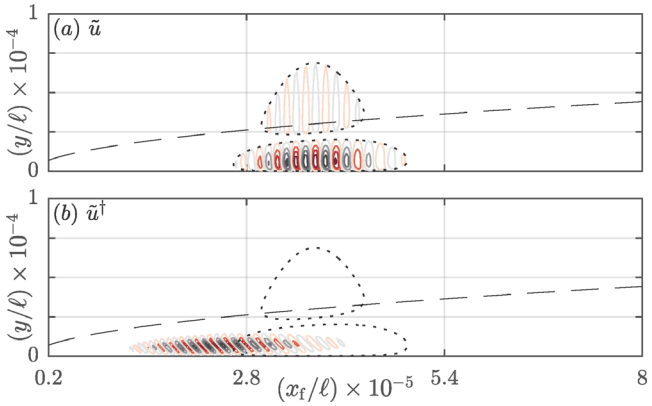

FIG. 10. (a) and (b) Isocontour of $|\tilde{u}|/|\tilde{u}|_{max}$ (dotted black, level: 1/9) and isocontours [colored lines, from minimum (gray) to maximum (red) with $\Delta = 2/9$] of (a) $\mathcal{R}\{\tilde{u}\}/|\tilde{u}|_{max}$ and (b) $\mathcal{R}\{\tilde{u}^\dagger\}/|\tilde{u}^\dagger|_{max}$ corresponding to the most unstable eigensolution at $c_f/u_e = 0.415$. $\bar{U} = 0.9u_e$-isocontour (dashed black).

TABLE III. Mode properties and relative errors ($\epsilon = |\omega_{ref} - \omega|/|\omega_{ref}|$) in the eigenvalue for the reference parameters: $x_{out}/\ell = 8.0 \times 10^5$; $N_x = 300$; Neumann in-/outflow boundary conditions; $y_{max}/\ell = 1.6 \times 10^5$, with respect to the (one at a time) parameter changes: $x_{out}/\ell = 7.0 \times 10^5$ (fixing the density N_x/L); $N_x = 260$; the use of Dirichlet in-/outflow boundary conditions; and $y_{max}/\ell = 1.4 \times 10^5$ (fixing $N_y = 50$ and $y_{i,1}/\ell = 4.0 \times 10^3$). First- and fifth-most unstable modes along the main branch for $c_f/u_e = 0.415$. The reported digits are truncated (not rounded) and those that are tainted by the largest reported error are underlined.

c_f/u_e	0.415	0.415
Mode #	1	5
$\omega_r\,\ell/u_e$	$-1.54607445982 \times 10^{-5}$	-1.48826×10^{-5}
$\omega_i\,\ell/u_e$	$+3.01443827834 \times 10^{-6}$	$+2.33523 \times 10^{-6}$
ϵ_L	1.4×10^{-4}	5.9×10^{-4}
ϵ_{N_x}	9.3×10^{-11}	2.5×10^{-7}
ϵ_{BC}	1.5×10^{-10}	2.0×10^{-6}
$\epsilon_{y_{max}}$	2.3×10^{-4}	2.2×10^{-4}

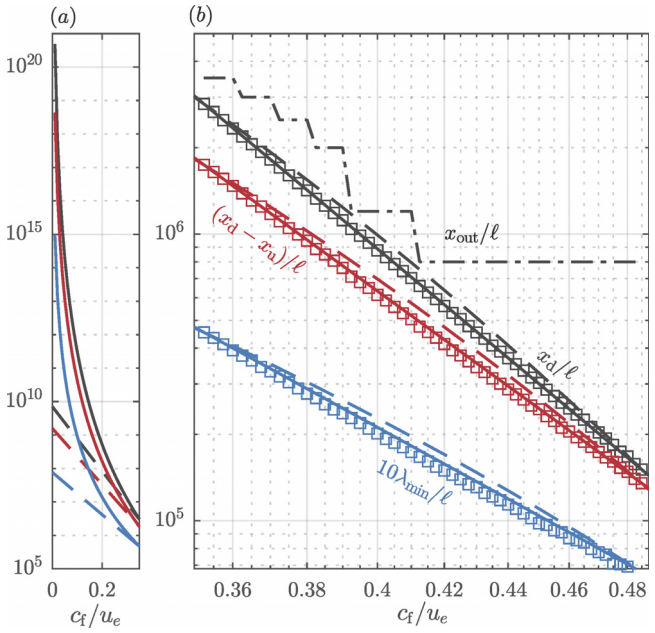

FIG. 11. For the most unstable $\tilde{u}$-eigenfunction: downstream extremum (x_d/ℓ, black), streamwise extent [$(x_d - x_u)/\ell$, red], and minimum wavelength ($10 \times \lambda_{min}/\ell$, blue) vs c_f. Measured values (symbols), power (solid lines), and exponential (dashed) fits and outflow boundary x_{out}/ℓ (dash-dotted). (a) Trend-extrapolation as $c_f \to 0$ (minimum: $0.025u_e$) and (b) data and fits.

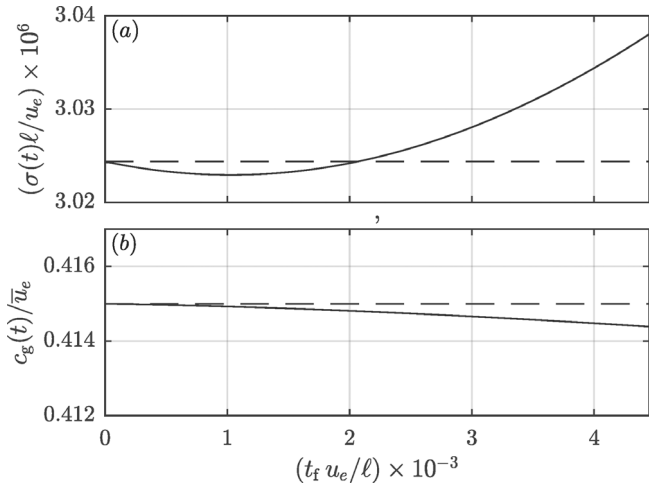

FIG. 12. (a) Temporal growth rate (measured with perturbation kinetic energy) in the stationary reference frame and (b) measured speed of the wave packets, initialized from most unstable eigenfunctions in moving frame of reference $c_f/u_e = 0.415$. Eigengrowth ω_i in (a) and frame speed c_f in (b) indicated by dashed lines.

that solving the moving-frame eigenvalue problem becomes more and more computationally demanding when lowering the frame speed. Extrapolation as $c_f \to 0$ of an exponential and power fit of the data given in Fig. 11(b) is illustrated in Fig. 11(a).

In order to carefully demonstrate that eigensolutions represent the (exact) instantaneous dynamics of the wave-packet solution to the initial-value problem at $t = 0$, without spurious transients, we show the short-time evolution of the wave packet in Fig. 12. We can thus verify that the moving-frame eigengrowth rate and the imposed frame speed are equal to the instantaneous growth rate and group speed of the temporal wave packet for $t = 0$, as indicated by Eqs. (19) and (20), respectively, and then slowly deviate for $t > 0$. This finding was confirmed for many different frame speeds and different modes for the same frame speed.

APPENDIX B: RECOVERING *N*-FACTOR AND NEUTRAL CURVES FOR THE BLASIUS BOUNDARY LAYER

As a verification, the present approach was also used to recover the traditional *N*-factor and neutral stability curves for the Blasius boundary layer for which accurate results can be obtained with PSE.

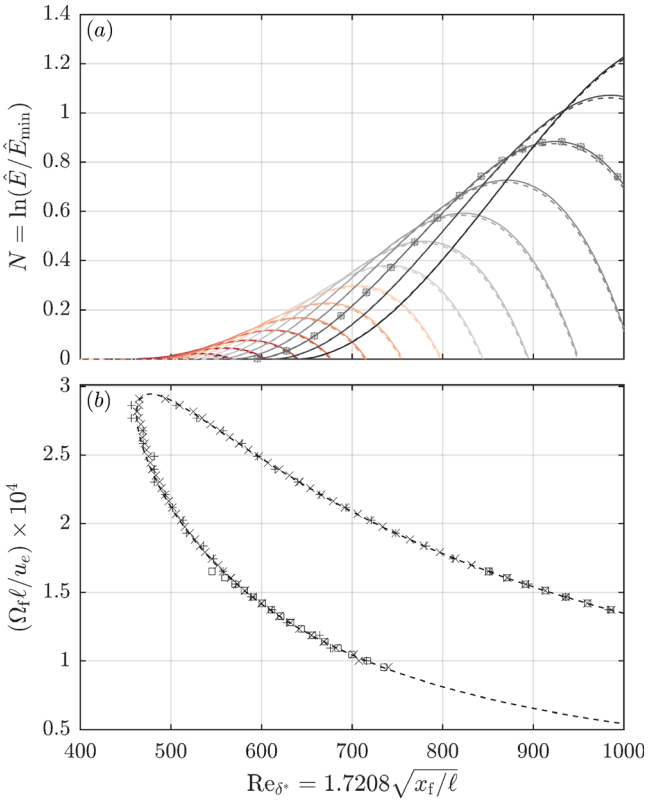

FIG. 13. Verification of the present time-dependent wave-packet approach (solid lines and/or symbols) vs PSE (dashed lines) for the Blasius boundary layer: (a) *N*-factor curves and (b) neutral curve with spatial growth based on kinetic energy $\hat{E}$. Crosses [and solid lines in (a)] and pluses: first- and second-most unstable modes for $c_f/u_e = 0.525$, respectively. Squares: most unstable mode for $c_f/u_e = 0.5$. In (a), angular frequencies are indicated by color level from $\Omega_f \ell/u_e = 1.256 \times 10^{-4}$ (gray) to 2.885×10^{-4} (red) with $\Delta\Omega_f \ell/u_e = 1.16 \times 10^{-5}$.

Since increasing the frame speed causes an upstream movement of the eigenfunctions, we can find eigenfunctions at $c_f/u_e = 0.525$ that are located far enough upstream of the neutral points for all relevant frequencies. By time-marching the most unstable eigensolution for this frame speed and Fourier transforming the resulting wave packet according to Eq. (21), the *N*-factor and neutral stability curves are recovered. The verification against PSE is shown in Fig. 13.

In addition to the aforementioned eigensolution, we furthermore time-marched other localized eigensolutions corresponding to the same frame speed ($c_f/u_e = 0.525$) and the most unstable solution for different frame speeds in order to verify that the *N*-factor and neutral stability curves do not depend on this selection. Figure 13 illustrates this verification for the results corresponding to the second-most unstable solution for $c_f/u_e = 0.525$ (pluses) and the most unstable solution for $c_f/u_e = 0.500$ (squares). The eigenfunctions for the latter solution are located farther downstream; hence, the verification can only be established from a farther downstream location onward.

REFERENCES

[1] J. Délery and J.-P. Dussauge, "Some physical aspects of shock wave/boundary layer interactions," Shock Waves **19**, 453–468 (2009).
[2] A. Ferri, "Experimental results with airfoils tested in the high-speed tunnel at Guidonia," Report No. NACA-TM-946 (National Advisory Committee for Aeronautics, 1939).
[3] C. d. Donaldson, "Effects of interaction between normal shock and boundary layer," Report No. NACA-CB-4A27 (National Advisory Committee for Aeronautics, 1944).
[4] H. W. Liepmann, "The interaction between boundary layer and shock waves in transonic flow," J. Aeronaut. Sci. **13**, 623–637 (1946).
[5] J. Ackeret, F. Feldmann, and N. Rott, "Investigations of compression shocks and boundary layers in gases moving at high speed," Report No. NACA-TM-1113 (National Advisory Committee for Aeronautics, 1947).
[6] A. Fage and R. F. Sargent, "Shock-wave and boundary-layer phenomena near a flat surface," Proc. R. Soc. London, Ser. A **190**, 1–20 (1947).
[7] J. Délery, J. G. Marvin, and E. Reshotko, "Shock-wave boundary layer interactions," Report No. ADA171302 (Advisory Group for Aerospace Research and Development, 1986).
[8] D. S. Dolling, "Fifty years of shock-wave/boundary-layer interaction research: What next?," AIAA J. **39**, 1517–1531 (2001).
[9] H. Babinsky and J. Harvey, *Shock wave–Boundary-Layer Interactions* (Cambridge University Press, Cambridge, 2011).
[10] D. V. Gaitonde, "Progress in shock wave/boundary layer interactions," Prog. Aerosp. Sci. **72**, 80–99 (2015).
[11] S. J. Beresh, N. T. Clemens, and D. S. Dolling, "Relationship between upstream turbulent boundary-layer velocity fluctuations and separation shock unsteadiness," AIAA J. **40**, 2412–2422 (2002).
[12] B. Ganapathisubramani, N. T. Clemens, and D. S. Dolling, "Effects of upstream boundary layer on the unsteadiness of shock-induced separation," J. Fluid Mech. **585**, 369–394 (2007).
[13] B. Ganapathisubramani, N. T. Clemens, and D. S. Dolling, "Low-frequency dynamics of shock-induced separation in a compression ramp interaction," J. Fluid Mech. **636**, 397–425 (2009).
[14] M. Wu and M. P. Martín, "Analysis of shock motion in shockwave and turbulent boundary layer interaction using direct numerical simulation data," J. Fluid Mech. **594**, 71–83 (2008).
[15] B. W. Tester, J. G. Coder, C. S. Combs, and J. D. Schmisseur, "Hybrid RANS/LES simulation of transitional shockwave/boundary-layer interaction," in Fluid Dynamics Conference, 2018.
[16] L. E. Lash, M. Gragston, P. A. Kreth, Z. McDaniel, J. G. Coder, and J. D. Schmisseur, "Upstream influence in shock wave/transitional boundary layer interactions at Mach 1.8," AIAA J. **59**, 4842–4857 (2021).

[17]N. F. Nutter, J. W. Cobourn, R. B. Bond, P. A. Kreth, J. D. Schmisseur, R. S. Glasby, D. L. Stefanski, E. Hereth, and J. G. Coder, "Simulations of dynamic shock wave/boundary layer interactions using HPCMP CREATE™-AV Kestrel COFFE," in AIAA Scitech 2021 Forum, 2021.
[18]J. J. Sebastian and F. K. Lu, "Upstream-influence scaling of fin-induced laminar shockwave/boundary-layer interactions," AIAA J. **59**, 1861–1864 (2021).
[19]E. Touber and N. D. Sandham, "Oblique shock impinging on a turbulent boundary layer: Low-frequency mechanisms," in *38th AIAA Fluid Dynamics Conference and Exhibit* (University of Southampton, Southampton, UK, 2008).
[20]E. Touber and N. D. Sandham, "Large-eddy simulation of low-frequency unsteadiness in a turbulent shock-induced separation bubble," Theor. Comput. Fluid Dyn. **23**, 79–107 (2009).
[21]S. Pirozzoli and F. Grasso, "Direct numerical simulation of impinging shock wave/turbulent boundary layer interaction at $M = 2.25$," Phys. Fluids **18**, 065113 (2006).
[22]J.-P. Dussauge, P. Dupont, and J. F. Debiève, "Unsteadiness in shock wave boundary layer interactions with separation," Aerosp. Sci. Technol. **10**, 85–91 (2006).
[23]S. Piponniau, J. P. Dussauge, J. F. Debiève, and P. Dupont, "A simple model for low-frequency unsteadiness in shock-induced separation," J. Fluid Mech. **629**, 87–108 (2009).
[24]M. Grilli, P. J. Schmid, S. Hickel, and N. A. Adams, "Analysis of unsteady behaviour in shockwave turbulent boundary layer interaction," J. Fluid Mech. **700**, 16–28 (2012).
[25]A. Sansica, N. D. Sandham, and Z. Hu, "Instability and low-frequency unsteadiness in a shock-induced laminar separation bubble," J. Fluid Mech. **798**, 5–26 (2016).
[26]V. Pasquariello, S. Hickel, and N. A. Adams, "Unsteady effects of strong shock-wave/boundary-layer interaction at high Reynolds number," J. Fluid Mech. **823**, 617–657 (2017).
[27]M. C. Adler and D. V. Gaitonde, "Dynamic linear response of a shock/turbulent-boundary-layer interaction using constrained perturbations," J. Fluid Mech. **840**, 291–341 (2018).
[28]K. Sasaki, D. C. Barros, A. V. G. Cavalieri, and L. Larchevêque, "Causality in the shock wave/turbulent boundary layer interaction," Phys. Rev. Fluid **6**, 064609 (2021).
[29]N. T. Clemens and V. Narayanaswamy, "Low-frequency unsteadiness of shock wave/turbulent boundary layer interactions," Annu. Rev. Fluid Mech. **46**, 469–492 (2014).
[30]A. Dwivedi, N. Hildebrand, J. W. Nichols, G. V. Candler, and M. R. Jovanović, "Transient growth analysis of oblique shock-wave/boundary-layer interactions at Mach 5.92," Phys. Rev. Fluids **5**, 063904 (2020).
[31]N. Bonne, V. Brion, E. Garnier, R. Bur, P. Molton, D. Sipp, and L. Jacquin, "Analysis of the two-dimensional dynamics of a Mach 1.6 shock wave/transitional boundary layer interaction using a RANS based resolvent approach," J. Fluid Mech. **862**, 1166–1202 (2019).
[32]B. Bugeat, J.-C. Robinet, J.-C. Chassaing, and P. Sagaut, "Low-frequency resolvent analysis of the laminar oblique shock wave/boundary layer interaction," J. Fluid Mech. **942**, A43 (2022).
[33]J. W. Nichols, J. Larsson, M. Bernardini, and S. Pirozzoli, "Stability and modal analysis of shock/boundary layer interactions," Theor. Comput. Fluid Dyn. **31**, 33–50 (2017).
[34]S. Pirozzoli, J. Larsson, J. Nichols, M. Bernardini, B. Morgan, and S. Lele, "Analysis of unsteady effects in shock/boundary layer interactions," in *Proceedings of the Summer Program* (Center for Turbulence Research, 2010), pp. 153–164.
[35]J. C. Robinet, "Bifurcations in shock-wave/laminar-boundary-layer interaction: Global instability approach," J. Fluid Mech. **579**, 85–112 (2007).
[36]N. J. Hildebrand, A. Dwivedi, J. W. Nichols, M. R. Jovanović, and G. V. Candler, "Simulation and stability analysis of oblique shock-wave/boundary-layer interactions at Mach 5.92," Phys. Rev. Fluids **3**, 013906 (2018).
[37]D. Rodríguez, E. M. Gennaro, and L. F. Souza, "Self-excited primary and secondary instability of laminar separation bubbles," J. Fluid Mech. **906**, A13 (2020).
[38]F. Guiho, F. Alizard, and J. C. Robinet, "Instabilities in oblique shock wave/laminar boundary-layer interactions," J. Fluid Mech. **789**, 1–35 (2016).
[39]Y. Yao, L. Krishnan, N. D. Sandham, and G. T. Roberts, "The effect of Mach number on unstable disturbances in shock/boundary-layer interactions," Phys. Fluids **19**, 054104 (2007).
[40]A. Sansica, N. D. Sandham, and Z. Hu, "Forced response of a laminar shock-induced separation bubble," Phys. Fluids **26**, 093601 (2014).
[41]V. Theofilis, "Advances in global linear instability analysis of nonparallel and three-dimensional flows," Prog. Aerosp. Sci. **39**, 249–315 (2003).
[42]K. J. Groot, "BiGlobal stability of shear flows spanwise & streamwise analyses," Ph.D. thesis (TU Delft and Von Karman Institute for Fluid Dynamics, 2018).
[43]U. Ehrenstein and F. Gallaire, "On two-dimensional temporal modes in spatially evolving open flows: The flat-plate boundary layer," J. Fluid Mech. **536**, 209–218 (2005).
[44]F. Alizard and J.-C. Robinet, "Spatially convective global modes in a boundary layer," Phys. Fluids **19**, 114105 (2007).
[45]D. A. Rodríguez, A. Tumin, and V. Theofilis, "Towards the foundation of a global modes concept," in *6th AIAA Theoretical Fluid Mechanics Conference* (American Institute of Aeronautics and Astronautics, Honolulu, HI (AIAA, 2011), pp. 1–18.
[46]K. J. Groot and H. M. Schuttelaars, "Accurate numerical approximation of the absolute stability of unbounded flows," Physica D **402**, 132224 (2020).
[47]S. Mittal and B. Kumar, "A stabilized finite element method for global analysis of convective instabilities in nonparallel flows," Phys. Fluids **19**, 088105 (2007).
[48]S. Mittal, J. J. Kottaram, and B. Kumar, "Onset of shear layer instability in flow past a cylinder," Phys. Fluids **20**, 054102 (2008).
[49]B. Kumar and S. Mittal, "On the origin of the secondary vortex street," J. Fluid Mech. **711**, 641–666 (2012).
[50]R. H. M. Giepman, "Flow control for oblique shock wave reflections," Ph.D. thesis (Delft University of Technology, 2016).
[51]S. Hickel, C. P. Egerer, and J. Larsson, "Subgrid-scale modeling for implicit large eddy simulation of compressible flows and shock-turbulence interaction," Phys. Fluids **26**, 106101 (2014).
[52]S. Niessen, "BiGlobal stability analysis: Laminar shock-wave/boundary-layer interactions," Master's thesis (Faculty of Applied Sciences, University of Liège, 2017).
[53]E. Åkervik, L. Brandt, D. S. Henningson, J. Hœpffner, O. Marxen, and P. Schlatter, "Steady solutions of the Navier-Stokes equations by selective frequency damping," Phys. Fluids **18**, 068102 (2006).
[54]B. E. Jordi, C. J. Cotter, and S. J. Sherwin, "Encapsulated formulation of the selective frequency damping method," Phys. Fluids **26**, 034101 (2014).
[55]J. Casacuberta, K. J. Groot, H. J. Tol, and S. Hickel, "Effectivity and efficiency of selective frequency damping for the computation of unstable steady-state solutions," J. Comput. Phys. **375**, 481–497 (2018).
[56]N. Cerulus, H. Quintanilha, and V. Theofilis, "Global linear stability analysis of the supersonic flows over a hollow cylinder flare model," in *AIAA Scitech Forum*, Reston, VA (American Institute of Aeronautics and Astronautics, 2021), p. 247.
[57]D. Chapman, D. Kuehn, and H. Larson, "Investigation of separated flow in supersonic and subsonic streams with emphasis of the effect of transition," Report No. 1356 (National Advisory Committee for Aeronautics, Ames Aeronautical Lab, Moffett Field, CA, 1958).
[58]M. P. Avanci, D. Rodríguez, and L. S. d. B. Alves, "A geometrical criterion for absolute instability in separated boundary layers," Phys. Fluids **31**, 014103 (2019).
[59]E. B. White, "Transient growth of stationary disturbances in a flat plate boundary layer," Phys. Fluids **14**, 4429–4439 (2002).
[60]Z. Huang and X. Wu, "A local scattering approach for the effects of abrupt changes on boundary-layer instability and transition: A finite-Reynolds-number formulation for isolated distortions," J. Fluid Mech. **822**, 444–483 (2017).
[61]L. Zhao, M. Dong, and Y. Yang, "Harmonic linearized Navier-Stokes equation on describing the effect of surface roughness on hypersonic boundary-layer transition," Phys. Fluids **31**, 034108 (2019).
[62]N. Hildebrand, M. M. Choudhari, and P. Paredes, "Predicting boundary-layer transition over backward-facing steps via linear stability analysis," AIAA J. **58**, 3728–3734 (2020).
[63]T. Appel, "Boundary layer instabilities due to surface irregularities: A harmonic Navier-Stokes approach," Ph.D. thesis (Imperial College London, 2020).

[64]M. M. Peck, K. J. Groot, and H. L. Reed, "Boundary-layer instability on a highly swept fin on a hypersonic cone," in *AIAA AVIATION 2022 Forum* (AIAA, 2022), p. 3555.
[65]K. J. Groot, "Derivation of and simulations with BiGlobal stability equations," Master's thesis (Delft University of Technology, 2013).
[66]W. S. Saric and A. H. Nayfeh, "Nonparallel stability of boundary-layer flows," Phys. Fluids **18**, 945–952 (1975).
[67]P. Huerre and P. A. Monkewitz, "Local and global instabilities in spatially developing flows," Annu. Rev. Fluid Mech. **22**, 473–537 (1990).
[68]F. P. Bertolotti, T. Herbert, and P. Spalart, "Linear and nonlinear stability of the Blasius boundary layer," J. Fluid Mech. **242**, 441–474 (1992).
[69]P. A. Monkewitz, P. Huerre, and J.-M. Chomaz, "Global linear stability analysis of weakly non-parallel shear flows," J. Fluid Mech. **251**, 1–20 (1993).
[70]C. Canuto, M. Y. Hussaini, A. Quarteroni, and T. A. Zang, *Spectral Methods, Fundamentals in Single Domains* (Springer, 2006).
[71]M. Malik, "Numerical methods for hypersonic boundary layer stability," J. Comput. Phys. **86**, 376–413 (1990).
[72]K. J. Groot, J. Serpieri, F. Pinna, and M. Kotsonis, "Secondary crossflow instability through global analysis of measured base flows," J. Fluid Mech. **846**, 605–653 (2018).
[73]B. T. Chu, "On the energy transfer to small disturbances in fluid flow (Part I)," Acta Mech. **1**, 215–234 (1965).
[74]L. Larchevêque, "Low- and medium-frequency unsteadinesses in a transitional shock–boundary reflection with separation," in *54th AIAA Aerospace Sciences Meeting*, San Diego, CA (American Institute of Aeronautics and Astronautics (AIAA 2016-1833), 2016), pp. 1–14.
[75]O. M. F. Browne, A. P. Haas, H. F. Fasel, and C. Brehm, "An efficient linear wavepacket tracking method for hypersonic boundary-layer stability prediction," J. Comput. Phys. **380**, 243–268 (2019).
[76]P. J. Schmid and D. S. Henningson, *Stability and Transition in Shear Flows* (Springer, 2001).
[77]I. P. Montero and F. Pinna, "Analysis of the instabilities induced by an isolated roughness element in a laminar high-speed boundary layer," J. Fluid Mech. **915**, A90 (2021).